

The SAMI Pilot Survey: Stellar Kinematics of Galaxies in Abell 85, 168 and 2399.

L. M. R. Fogarty^{1,2*}, N. Scott^{1,2}, M. S. Owers^{3,4}, S. M. Croom^{1,2}, K. Bekki⁵, R. C. W. Houghton⁶, J. van de Sande¹, F. D'Eugenio⁷, G. N. Cecil⁸, M. M. Colless⁷, J. Bland-Hawthorn¹, S. Brough⁴, L. Cortese⁹, R. L. Davies⁶, D. H. Jones^{10,3}, M. Pracy¹, J. T. Allen^{1,2}, J. J. Bryant^{1,2,4}, M. Goodwin⁴, A. W. Green⁴, I. S. Konstantopoulos⁴, J. S. Lawrence⁴, N. P. F. Lorente⁴, S. Richards^{1,2,4}, R. G. Sharp⁸

¹ *Sydney Institute for Astronomy, School of Physics, University of Sydney, NSW 2006, Australia.*

² *ARC Centre of Excellence for All-Sky Astrophysics (CAASTRO).*

³ *Department of Physics and Astronomy, Macquarie University, NSW 2109, Australia.*

⁴ *Australian Astronomical Observatory, PO Box 915, North Ryde, NSW 1670, Australia.*

⁵ *ICRAR M468, The University of Western Australia, 35 Stirling Hwy, Crawley, Western Australia, 6009, Australia.*

⁶ *Astrophysics, Department of Physics, University of Oxford, Denys Wilkinson Building, Keble Rd., Oxford, OX1 3RH, UK.*

⁷ *Research School of Astronomy and Astrophysics, Australian National University, Canberra ACT 2611, Australia.*

⁸ *Department of Physics and Astronomy University of North Carolina Chapel Hill, NC 27599 USA.*

⁹ *Centre for Astrophysics and Supercomputing, Swinburne University of Technology, Hawthorn, VIC 3122, Australia.*

¹⁰ *School of Physics, Monash University, Clayton, VIC 3800, Australia.*

30 August 2024

ABSTRACT

We present the SAMI Pilot Survey, consisting of integral field spectroscopy of 106 galaxies across three galaxy clusters, Abell 85, Abell 168 and Abell 2399. The galaxies were selected by absolute magnitude to have $M_r < -20.25$ mag. The survey, using the Sydney-AAO Multi-object Integral field spectrograph (SAMI), comprises observations of galaxies of all morphological types with 75% of the sample being early-type galaxies (ETGs) and 25% being late-type galaxies (LTGs). Stellar velocity and velocity dispersion maps are derived for all 106 galaxies in the sample.

The λ_R parameter, a proxy for the specific stellar angular momentum, is calculated for each galaxy in the sample. We find a trend between λ_R and galaxy concentration such that LTGs are less concentrated higher angular momentum systems, with the fast-rotating ETGs (FRs) more concentrated and lower in angular momentum. This suggests that some dynamical processes are involved in transforming LTGs to FRs, though a significant overlap between the λ_R distributions of these classes of galaxies implies that this is just one piece of a more complicated picture.

We measure the kinematic misalignment angle, Ψ , for the ETGs in the sample, to probe the intrinsic shapes of the galaxies. We find the majority of FRs (83%) to be aligned, consistent with them being oblate spheroids (i.e. disks). The slow rotating ETGs (SRs), on the other hand, are significantly more likely to show kinematic misalignment (only 38% are aligned). This confirms previous results that SRs are likely to be mildly triaxial systems.

Key words: techniques: imaging spectroscopy – galaxies: kinematics and dynamics – galaxies: clusters

1 INTRODUCTION

Galaxies take many shapes, ranging from grand design spirals to smooth featureless ellipticals to highly irregular galax-

* l.fogarty@physics.usyd.edu.au

ies. Since shape is a readily apparent property, it has long been used to classify galaxies (e.g. Hubble 1926; de Vaucouleurs 1959). Early-type galaxies (ETGs) typically include those with featureless light profiles, the disk lenticulars (S0s) and the round ellipticals (Es). Conversely, the late-type galaxies (LTGs) are characterised by their spiral arm structure (tightly to loosely wound, Sa–Sd), sometimes seen with an accompanying bar (SBa–SBd).

The morphology-density relation (Dressler 1980; Houghton 2015) shows that ETGs are found in higher relative numbers in regions of higher galaxy density, such as massive clusters. This trend is mostly driven by an increase in the number density of S0 galaxies at the expense of LTGs, prompting many studies of the transformation from LTGs to S0s. There are many mechanisms by which such transformations can occur, such as ram-pressure stripping, which removes gas from the galaxy (Gunn & Gott 1972); tidal encounters (Icke 1985; Bekki & Couch 2011); truncation of the gas envelope, so that the remaining gas supply is rapidly consumed by SF without replenishment (known as strangulation) (Larson et al. 1980; Bekki et al. 2002); and minor mergers (Bekki 1998).

Different transformation mechanisms affect galaxies in different ways. However, morphology does not map to particular physical processes in a straightforward way. ETGs have been shown to exhibit a wide range of kinematic morphologies (Krajnović et al. 2011) and this can provide some clues as to their formation histories. The λ_R parameter is a proxy for the specific stellar angular momentum of a galaxy (Emsellem et al. 2007, 2011), and is measured from 2D kinematic maps. Separating ETGs according to λ_R yields two broad categories: fast and slow rotators (FRs/SRs). FRs and SRs have very different distributions in both angular momentum and intrinsic shape (Cappellari et al. 2011b; Weijmans et al. 2014) and likely form differently.

Establishing the different processes by which galaxies are transformed from LTGs to FRs, or from FRs or LTGs to SRs, is crucial to our understanding of galaxies. Large galaxy surveys using integral field spectroscopy (IFS), and with no morphological pre-selection, are needed to disentangle the different physical processes governing galaxy transformations. Observations of galaxy morphology are not enough - the addition of kinematic information provides a vital piece of the puzzle. In this paper we present the SAMI Pilot Survey, an IFS survey of 106 galaxies in three galaxy clusters. With this rich data set we explore evolutionary links between LTGs and FRs and the intrinsic structural differences between FRs and SRs.

The SAMI Pilot Survey is a precursor to the full SAMI Galaxy Survey¹ (Bryant et al. 2015) which will build a sample of ~ 3400 galaxies over three years, each with IFS data. This large and complex data set will enable us to build on the work presented here and give a unique perspective to the way we think about galaxy evolution.

In Section 2 we present our data and in Section 3 we validate our data reduction and analysis pipelines by comparing to previously published observations. In Section 4 we discuss some derived photometric parameters, such as measurements of the effective radius and ellipticity of the galaxies in our

sample, which we use in our analysis. In Section 5 we examine the distribution of angular momentum in our sample and in Section 6 we discuss the kinematic alignment of our sample. We discuss our results in Section 7 and conclude in Section 8.

2 OBSERVATIONS AND DATA

2.1 The SAMI Pilot Survey

The Sydney–AAO Multi-object IFS (SAMI) is a fibre-fed multi-object IFS on the Anglo–Australian Telescope (AAT) (Croom et al. 2012) capable of observing 13 galaxies at once. This has enabled an order of magnitude increase in survey speed compared to surveys using single object IFS. SAMI is based on lightly-fused fibre bundles called hexabundles (Bland-Hawthorn et al. 2011; Bryant et al. 2011, 2014), with 13 hexabundles deployable across a one-degree field of view. Each SAMI hexabundle consists of 61 optical fibres arranged in a circular pattern with a mean fill factor of 73%. Each fibre is 1.6'' in diameter and each hexabundle is $\sim 15''$ in diameter on sky. SAMI is mounted on the triplet top-end of the AAT and feeds the AAOmega spectrograph (Smith et al. 2004; Sharp et al. 2006). AAOmega is a fully-configurable, double-beamed spectrograph. For general operations SAMI uses the low resolution 580V grating in the blue arm which delivers wavelength coverage in the range 3700–5700Å at a resolution $R \sim 1700$. In the red arm we use the medium resolution 1000R grating which delivers wavelength coverage in the range 6200–7300Å at a resolution $R \sim 4500$. This ensures the main stellar absorption features are covered in the blue while allowing precise emission line observations around H α in the red.

The SAMI Pilot Survey is a precursor to the SAMI Galaxy Survey and is focussed on galaxies in clusters. The cluster sample was selected from the X-ray cross-matched cluster catalogue of Wang et al. (2011). Within this catalogue suitable clusters were constrained to lie at $z < 0.06$ and at declination $< 10^\circ$ so as to be observable from Siding Spring Observatory, with a total of seven clusters selected. Target galaxies were then selected from the NYU Value-Added Galaxy Catalogue (Blanton et al. 2005) to be within a 1-degree radius of the cluster centre, and to be at $0.025 < z < 0.085$. Initially galaxies within a redshift range of $\pm dz = 0.01$ of the cluster redshift were defined (conservatively) as cluster members and were the highest priority targets. This definition of membership was for target selection only and was later refined for the purposes of fulfilling our scientific aim (Fogarty et al. 2014).

All galaxies with $M_r < -20.25$ mag were included in the full parent sample. Absolute magnitudes are from Blanton et al. (2005) and use a Λ CDM cosmology such that $\Omega_M = 0.3$, $\Omega_\Lambda = 0.7$ and $H_0 = 100 \text{ km s}^{-1} \text{ Mpc}^{-1}$. Cluster member galaxies meeting the conservative criteria above were prioritised according to absolute magnitude, with the brightest objects ($M_r < -21.68$ mag) having highest priority, objects with $M_r < -20.5$ mag having intermediate priority and objects with $-20.5 \text{ mag} < M_r < -20.25$ mag having lower priority. Foreground and background galaxies around the cluster were similarly ranked by absolute magnitude (but all at a lower priority than the cluster galaxies). Of the se-

¹ <http://sami-survey.org/>

lected clusters three were observed, Abell 85, Abell 168, and Abell 2399.

2.2 Sampling and Completeness

The SAMI Pilot Survey was completed over two separate observing runs from 10th–13th September and 11th–16th October 2012. Not all 13 SAMI hexabundles were in use at this time due to hardware issues that were rectified after the October 2012 run. During the Pilot Survey fourteen fields, containing eight galaxies each, were observed. A ninth hexabundle was allocated to a secondary standard star for calibration purposes. In total 112 galaxies were observed. However, due to astrometric errors during the September 2012 run the data for six of these proved unusable. The final sample is therefore 106 galaxies (97 cluster members and 9 foreground/background objects) from three cluster fields of Abell 85, Abell 168 and Abell 2399.

No morphological pre-selection was made and so all morphological types are included in our sample. The sample was classified visually using imaging into two morphological classes, ETGs and LTGs. For our purposes ETGs are objects with a smooth symmetrical light distribution without spiral structure or prominent dust lanes. All other galaxies are classified as LTGs (these are all spirals in our sample). A breakdown of the sample properties is given in Table 1. As the sample is dominated by cluster member galaxies the majority of galaxies in the sample are ETGs. Throughout this paper the terms ETG and LTG refer only to this visual morphological classification.

At the sample selection and observation stage a simple estimate of cluster membership was made and so the final sample contains some foreground and background objects. Once the SAMI observations were complete a programme was undertaken to increase the spectroscopic completeness of the parent sample and to define cluster membership more precisely. The SAMI Cluster Redshift Survey (Owers et al. in prep.) used the 2dF + AAOmega spectrograph on the AAT for 7 nights in September 2013. Redshifts were measured for ~ 1600 cluster members within R_{200} , the cluster radius at which the density is 200 times the critical density of the Universe at that redshift, across 8 galaxy clusters including Abell 85, Abell 168 and Abell 2399. This enabled a robust measurement of cluster membership. The method used is described in detail in Owers et al. in prep., with an overview given in Fogarty et al. (2014).

It is important that our sample of 97 cluster member galaxies is not biased such that we preferentially observe galaxies with a particular kinematic class (Houghton et al. 2013). This is particularly important when classifying the 74 ETGs in our cluster sample as FRs/SRs as SRs tend to be high mass (more luminous) galaxies, rounder than FRs (most SRs have ellipticity less than 0.4). To check for bias in our sample of 97 cluster members we compare the observed sample to the parent sample of cluster members from the original input catalogue, paying particular attention to potential bias in absolute magnitude and ellipticity distributions.

The distribution of r -band absolute magnitude (M_r) is shown in Figure 1. Two comparisons are made, first including the low priority targets (those with $-20.5 \text{ mag} < M_r < -20.25 \text{ mag}$) and second considering only the high

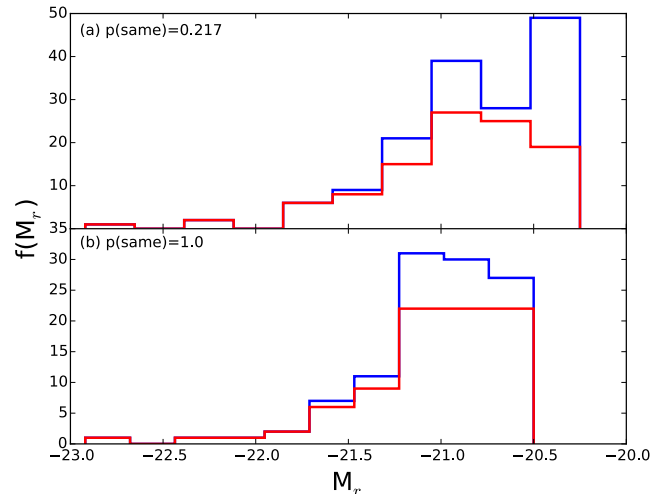


Figure 1. The absolute r -band magnitude distribution of the parent cluster member sample selected from the NYU-VAGC (Blanton et al. 2005) is shown in blue, with the observed SAMI Pilot cluster member galaxies shown in red. Panel (a) uses the parent sample with a cut-off of $M_r < -20.25$, including lower priority galaxies. Panel (b) shows just the high priority objects with $M_r < -20.5$. In both cases a K-S test convincingly shows that there is no measurable bias in our observed sample.

priority targets (i.e. with $M_r < -20.5 \text{ mag}$). In the first case a Kolmogorov–Smirnov (K–S) test yields a p-value of 0.217 meaning that we cannot reject the null hypothesis that the two distributions are drawn from the same parent sample. In the case of the high priority targets the p-value is 1.0. It is not surprising that the p-value should be lower in the case where we include the lower priority targets. However, in both cases it is clear that there is no measurable bias in our observed sample. The distribution of ellipticities is shown in Figure 2 with the panels as per Figure 1. For both cases the p-values is 1.0 and this convincingly shows that our sample is not biased in ellipticity.

2.3 Test Galaxy Observations

To validate our data reduction and analysis procedures we compare SAMI observations with already public IFS data. The ATLAS^{3D} survey (Cappellari et al. 2011a) provides a useful sample for comparison. The stellar kinematics for the 260 ETGs observed for the ATLAS^{3D} survey and presented in Krajnović et al. (2011) are now public.

During the SAMI Pilot Survey run in October 2012 we observed two galaxies from the ATLAS^{3D} sample, NGC1289 and NGC1665. These galaxies are not typical SAMI Pilot Survey or SAMI Galaxy Survey targets, being much more local and therefore larger on the sky. Both galaxies significantly overfill the SAMI hexabundle field of view. Despite this, these observations do give us the opportunity to test whether we can reproduce previously known results with our instrument, observation procedure, and data reduction and analysis tools. Details of our test galaxy observations are given in Table 2.

Both NGC1289 and NGC1665 were observed using a single hexabundle in SAMI, with the other hexabundles observing blank sky. This is not the normal operating proce-

Cluster Name	Cluster Redshift	ETGs		LTGs	
		Members	Non-members	Members	Non-members
Abell 85	0.0549	28	0	2	0
Abell 168	0.0451	12	0	11	1
Abell 2399	0.0583	34	5	10	3

Table 1. A summary of the galaxies observed in the SAMI Pilot Survey. The majority ($\sim 75\%$) of the sample comprises ETGs, with the remaining $\sim 25\%$ being LTGs. There are only 9 cluster non-members observed.

Galaxy	R.A. (J2000) (degrees)	Dec. (J2000) (degrees)	Distance (Mpc)	Date Observed	Exposure Time
NGC1289	49.707542	-1.973333	38.4	14th October 2012	2 x 900s
NGC1665	72.071142	-5.427607	37.5	15th October 2012	3 x 900s

Table 2. The two galaxies selected from the ATLAS^{3D} survey and observed with SAMI in October 2012 as part of data validation tests. Distances are taken from Cappellari et al. (2011a).

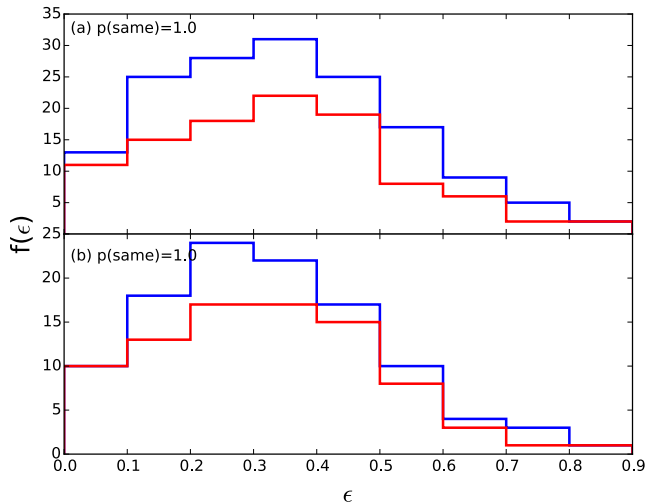


Figure 2. The ellipticity distribution of the parent cluster member sample selected from the NYU-VAGC (Blanton et al. 2005) is shown in blue, with the observed SAMI Pilot cluster member galaxies shown in red. Panels are as for Figure 1 with the full sample shown in panel (a) and the high priority bright sample shown in panel (b). Again, there is no measurable bias in our observed sample.

procedure for SAMI and led to some subtle differences in the data processing. These are described in detail in Section 2.4.

2.4 SAMI Data Reduction

The data reduction procedure for the SAMI Pilot survey is similar to that for the full SAMI Galaxy Survey (Allen et al. 2015; Sharp et al. 2015), but differs in a few small ways. This is due mainly to the nature of the SAMI Pilot Survey observations which used a less uniform dither pattern (i.e. different for different fields). The SAMI Pilot Survey data are of lower quality than the SAMI Galaxy Survey data as an instrument upgrade was performed between the two surveys, significantly improving the throughput of the instrument [see Bryant et al. (2015) for details]. Here we briefly describe the

data reduction procedure and the areas where the SAMI Pilot Survey data and our test data are treated differently.

The raw SAMI data are initially processed using the 2DFDR² package (Sharp & Birchall 2010). For each raw frame, the output from 2DFDR is a reduced row stacked spectrum (RSS) frame with all 819 SAMI fibre spectra bias subtracted, flat-fielded, wavelength calibrated and sky subtracted. The remaining reduction steps are performed using the custom-written SAMI python package (Allen et al. 2014). After the RSS data are produced, a spectrophotometric standard star is used to flux calibrate data. The variance for each fibre spectrum is correctly propagated through these steps.

As the fill factor of the SAMI hexabundles is not 100%, the standard observing procedure is to dither the observations, filling in the gaps between fibres and gaining spatial resolution (Sharp et al. 2015). Each dither yields a single RSS file, all of which must then be combined to form a uniformly sampled data cube for each galaxy. For the SAMI Pilot Survey the dither pattern used was non-standard. A different set of parameters to those used for the SAMI Galaxy Survey is therefore adopted when resampling the SAMI Pilot Survey data cubes. Similarly for the test galaxy data cubes, a unique set of resampling parameters are used, suitable for these data only.

To resample the SAMI RSS frames to uniform data cubes we use an algorithm similar to Drizzle (Fruchter & Hook 2002). The procedure, fully described in Sharp et al. (2015), is based on two parameters: a drop factor and output grid sampling. The drop factor is used to “shrink” the round footprint of the input fibres, conserving flux density. The new shrunk footprint is drizzled onto an output grid of square spaxels, the size of which is given by the output grid sampling. The SAMI Pilot Survey uses a drop factor of 0.75 and an output grid sampling of $0.5''$ per spaxel. For the test galaxies the observation procedure is very tailored. Notably there are only 2 and 3 dithers for NGC1289 and NGC1665 respectively, and so a drop factor of 1.0 is chosen to minimise gaps in coverage. Because of the large drop size the output

² <http://www.aao.gov.au/science/software/2dfdr>

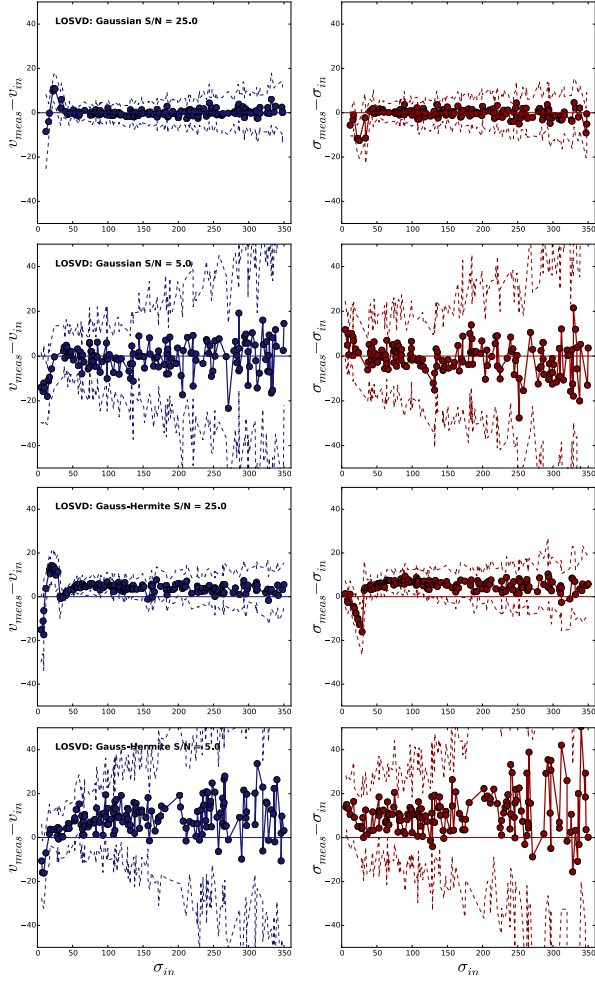


Figure 3. Results from simulated LOSVD fitting with pPXF. The top four panels show the simulations using a Gaussian LOSVD as input, for a spectrum with S/N=25 (top row) and one with S/N=5 (second row). The bottom four panels show the simulations using a Gauss-Hermite LOSVD, for a spectrum with S/N=25 (third row) and one with S/N=5 (bottom row). In all cases the blue points show the difference between the input velocity and the measured velocity as a function of input velocity dispersion. The red points show the difference between the input velocity dispersion and the measured velocity dispersion. The solid horizontal line indicated zero and the dashed lines show the one-sigma uncertainties.

grid sampling is also chosen to be large, $1''$ per spaxel to minimise covariance between spatial pixels.

When resampling the SAMI RSS frames onto regularly gridded data cubes it is important to correctly align the individual dithers with one another. This step is performed using fits to the secondary standard star which is observed simultaneously with all galaxy fields in the SAMI Pilot Survey (see Allen et al. (2015) for details). However, our test data have no such secondary star. Instead the alignment between RSS frames is found by fitting the position of the galaxy in each frame, using a two-dimensional Gaussian profile, and registering them according to the fit positions. Since both test galaxies are very bright and are smooth regular objects this procedure works well. Atmospheric dispersion is neglected

for the test galaxy observations, but this does not impact our results.

2.5 Stellar Kinematics of galaxies in Abell 85, Abell 168 and Abell 2399

We use the penalised pixel-fitting routine (pPXF) developed by Cappellari & Emsellem (2004) to fit stellar templates to the SAMI Pilot Survey galaxies. The procedure we followed is described below.

For each galaxy a spectrum is extracted from a central circular aperture with a $6''$ radius. This spectrum is fit using pPXF and the 985 MILES stellar templates (Sánchez-Blázquez et al. 2006) (with a fourth order additive polynomial) determining the best fit set of templates for that spectrum. The weighted and combined best fit template is then fit (again with a fourth order additive polynomial) to every spaxel in the data cube that meets the criterion of $S/N \geq 5$ in the continuum. The S/N is measured across a narrow wavelength range ($\sim 200 \text{ \AA}$) in a relatively flat part of the spectrum defined in pixel space and corresponding to between 4716 \AA and 4928 \AA for the lowest redshift object in our sample and 4913 \AA and 5134 \AA for the most distant. In all fits the emission lines are clipped using the *clean* option in pPXF. This works well for the SAMI Pilot Survey galaxies as none contain broad emission lines with significant wings.

The S/N threshold was chosen to balance the need for spatial coverage in the outskirts of the galaxies in the sample with the need for high quality kinematic measurements. If the S/N threshold is too low we risk measuring kinematics that are systematically biased. To test this we construct a set of spectra with fixed S/N values and convolved the spectra with a known LOSVD, parametrised by either a Gaussian or by a Gauss-Hermite series, with four moments (van der Marel & Franx 1993; Gerhard 1993):

$$L_{gh}(v) = \frac{1}{\sigma\sqrt{2\pi}} e^{-\frac{(v-V)^2}{2\sigma^2}} \left[1 + \sum_{m=3}^4 h_m H_m(y) \right] \quad (1)$$

Both the Gaussian and Gauss-Hermite LOSVDs are constructed with no velocity shift, for simplicity. The latter uses higher order moments $h_3 = h_4 = 0.1$. For both versions of the LOSVD the input velocity dispersion is varied between $5 - 350 \text{ km s}^{-1}$. A template spectrum is constructed by fitting the central aperture spectrum of one of the SAMI Pilot Survey galaxies (J004001.68-095252.5) using the MILES spectral library. The MILES spectra chosen by pPXF are combined to create a single infinite S/N spectrum with no intrinsic stellar velocity dispersion. Gaussian noise is then added to create spectra with the desired S/N, in this case we tested S/N values of 25 and 5. We then measure the kinematics of the resulting spectra in the same way as for the SAMI Pilot Survey data, fitting for all four moments (V , σ , h_3 and h_4) using the automatic bias setting in pPXF (Cappellari & Emsellem 2004).

The results are shown in Figure 3 for the Gaussian LOSVD and an input S/N of 25 and 5 (top four panels). At S/N=25 we do not find any systematic offsets in the recovered velocity and velocity dispersion down to an input dispersion of about 30 km s^{-1} . At a S/N of 5 the V and σ values are also recovered without systematic errors, though

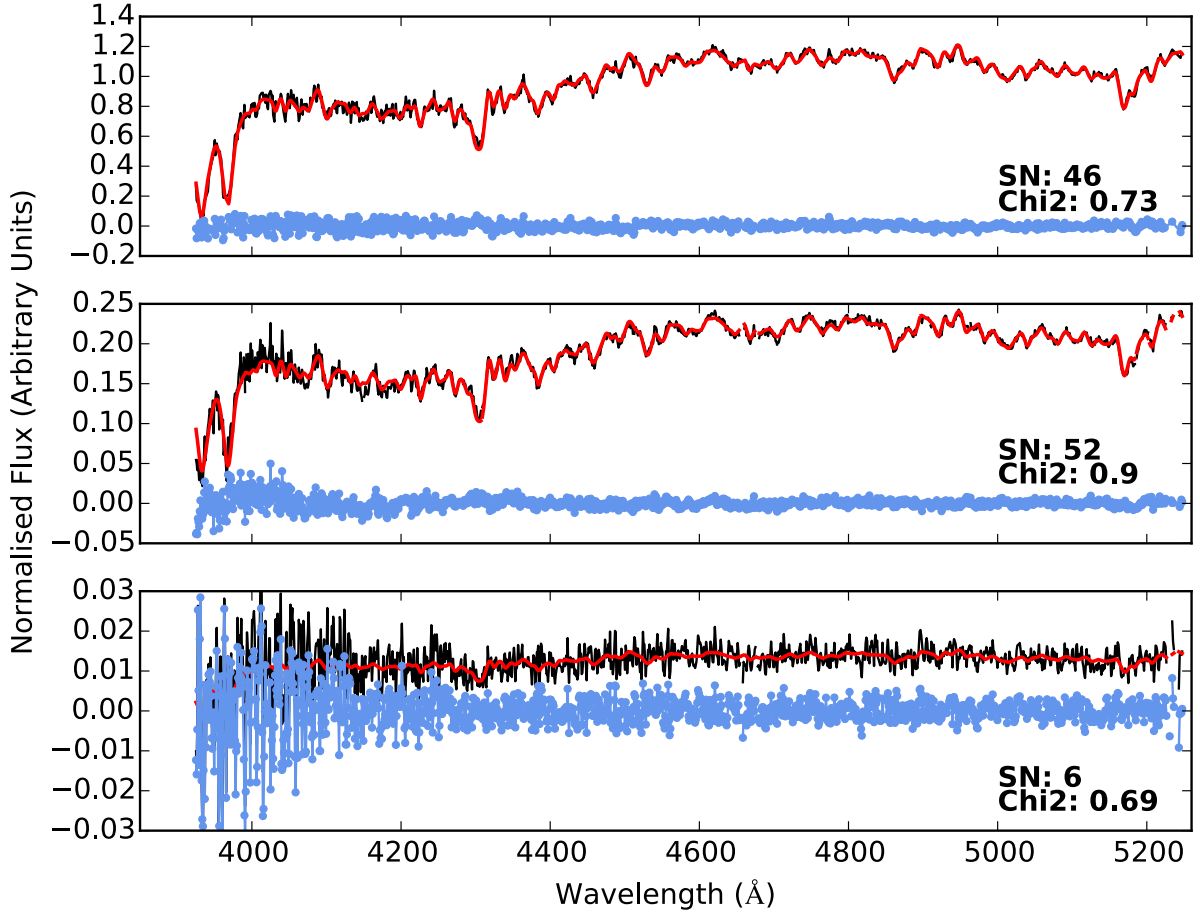


Figure 4. Three SAMI spectra with pPXF fits are shown for the galaxy J004001.68-095252.5. In the top panel the integrated aperture spectrum (from a $6''$ radius circular aperture) is shown in black, with the pPXF fit in red and the residuals in blue. The centre panel shows a single spaxel spectrum from the centre of the galaxy, with high S/N. The bottom panel shows a lower S/N spectrum from the outskirts of the galaxy, with S/N close to our chosen threshold of 5. The low S/N spectrum shows a good fit above 4100 \AA but with increased noise below.

the random errors are larger when compared with the values recovered from the spectrum with $S/N=25$.

If we assume a Gauss-Hermite LOSVD (Figure 3, bottom four panels) the recovered values show a small systematic bias in V and σ on the order of $\sim 5 - 10 \text{ km s}^{-1}$. This is due to the pPXF penalising bias setting not being perfectly tuned to the data. However, this is a small effect and our simulations show we are dominated by random errors, not systematic errors. For our purposes we assume that the LOSVD is Gaussian and accept that if this assumption is not always correct we introduce a small error in the measurements.

The central aperture radius, which is used to determine the optimal template for each galaxy, was chosen to account for strong stellar population gradients present in some of the LTGs in the sample. Fogarty et al. (2014) used a $2''$ radius central aperture spectrum, which may not represent the entire galaxy. This method is fine for ETGs, which tend to display a weak stellar population gradient, if any. To investigate whether template mismatch affects the kinematics for our sample we test two central apertures to determine the best fit template, a central $2''$ radius aperture and a $6''$ radius aperture covering the whole galaxy. We make this

comparison for all 106 galaxies, comparing the resulting velocity dispersion maps to search for a systematic bias. In the majority of cases the kinematic maps are the same within the errors. However, in eight of the LTGs (30%) a systematic bias in σ is seen. The offset is small ($< 10 \text{ km s}^{-1}$) and within the random error for most galaxies, but for those with the strongest radial colour gradients a systematic bias of greater than 20 km s^{-1} is seen. Template mismatch is a measurable problem for about half the LTGs in our sample. Using a large aperture to determine the best fit templates mediates this issue somewhat. For this reason we use the $6''$ radius aperture spectrum to determine the optimal template for all galaxies in the sample when extracting kinematics. This has a small impact on values derived from the kinematic maps, such as the kinematic PA and λ_R . The latter values are therefore different to those reported in Fogarty et al. (2014) for the ETGs. This is briefly discussed in Section 4.3

Some typical pPXF fits are shown in Figure 4 for the ETG J004001.68-095252.5. The top panel shows the fit to the central spectrum, extracted in a $6''$ radius circular aperture centred on the galaxy. The S/N in this spectrum is 46 and the fit is good, with a value of $\chi_{red}^2 = 0.73$. The centre and bottom panels of Figure 4 show single spaxel spectra from

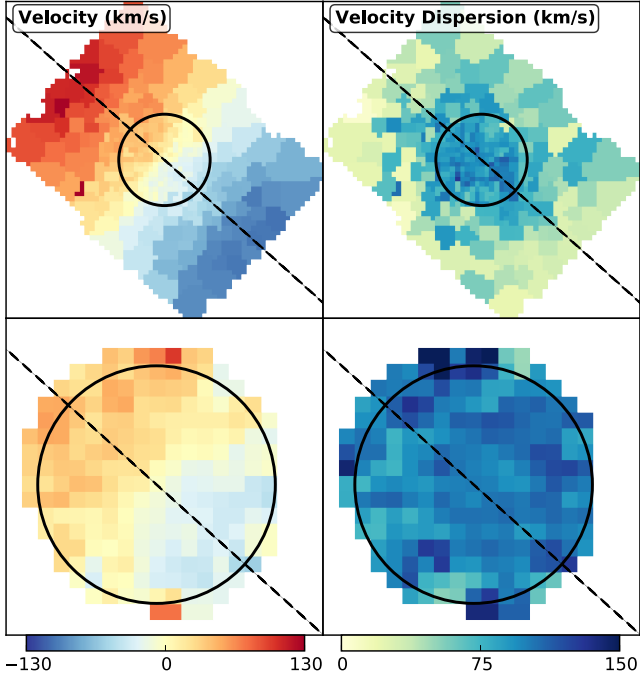


Figure 5. The stellar kinematics maps of NGC1665 from the ATLAS^{3D} survey (top row) and from SAMI (bottom row). In each panel North is up and East to the left. The left hand columns shows the velocity maps, scaled to $\pm 130 \text{ km s}^{-1}$ and the right-hand column shows the velocity dispersion, scaled to $0 - 150 \text{ km s}^{-1}$. The circle shows the SAMI hexabundle field of view, with a diameter of $\sim 15''$ and the dashed line shows the PA along which the profiles in Figure 6 are extracted. The structure in the SAMI maps matches that in the ATLAS^{3D} maps.

the data cube of the same galaxy. The centre panel shows a high S/N spectrum from the central part of the galaxy, where the pPXF fit is still very good, with a $\chi_{red}^2 = 0.9$. The lower panel shows a spectrum near to our S/N cut-off criterion. The fit to this spectrum has a lower value of $\chi_{red}^2 = 0.69$. This spectrum is much noisier than the others, especially at wavelengths shorter than 4100 \AA where there is essentially no signal.

The same procedure is used to extract stellar kinematics for NGC1289 and NGC1665.

3 DATA VALIDATION

As with any new instrument it is extremely important that we validate our observations by studying previously observed objects with published measurements. To do this we observed two test galaxies drawn from the ATLAS^{3D} sample (Cappellari et al. 2011a). These are NGC1665 and NGC1289. The SAMI observations of these galaxies are compared to publicly available data from ATLAS^{3D}.

Two nearby ETGs selected from the ATLAS^{3D} survey sample were observed with a single SAMI hexabundle in October 2012. Emsellem et al. (2011) classify NGC1665 as a FR with NGC1289 classified as a SR. Details of the SAMI observations for each galaxy are given in Table 2. These galaxies are not typical SAMI targets, being much larger on sky. Thus we are only able to probe the inner parts of these objects as

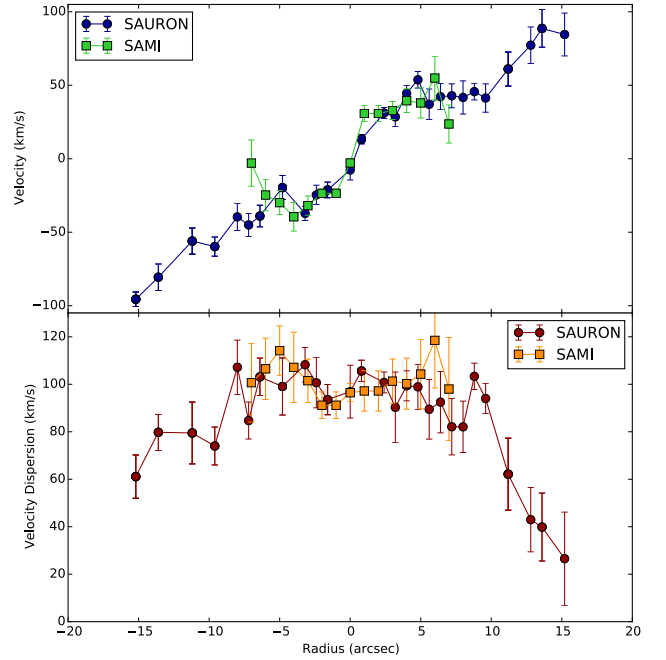


Figure 6. Radial profiles of the kinematics of NGC1665 from the ATLAS^{3D} survey and from SAMI. The top panel shows the rotation curve derived from ATLAS^{3D} in dark blue circles and from SAMI in light green squares. The bottom panel shows the velocity dispersion profile derived from ATLAS^{3D} in dark red circles and from SAMI in orange squares.

compared to the broader view afforded by the $33'' \times 41''$ SAURON IFS observations (Bacon et al. 2001) used for the ATLAS^{3D} survey. Nonetheless a valuable comparison of the galaxy centres can be made.

3.1 NGC1665

The kinematic maps for NGC1665 are shown in Figure 5. Data from the ATLAS^{3D} survey is shown on the top row and our new SAMI observations are on the bottom row. The velocity maps are on the left, with velocity dispersion on the right. The colour scaling is the same for corresponding ATLAS^{3D} and SAMI maps. A qualitative examination of the maps shows that the structure in the SAMI and ATLAS^{3D} data is very similar.

We also produce radial profiles of velocity and velocity dispersion from the ATLAS^{3D} and SAMI maps, shown in Figure 6. The profiles are extracted by plotting every spaxel which intersects a line defined by the photometric position angle of the galaxy, as given in Cappellari et al. (2011a). The line is shown as a dashed black line in Figure 5. The rotation curves are shown in the top panel. Within the SAMI field of view ($\sim \pm 7.5''$) the ATLAS^{3D} and SAMI curves agree well, within the errors, with both curves reaching $\pm 50 \text{ km s}^{-1}$. The same is true for the velocity dispersion profiles shown in the bottom panel of Figure 6. In this case the SAMI observations do not extend to the fall off seen by ATLAS^{3D} at $\sim \pm 10''$. However, in the central region both SAMI and ATLAS^{3D} see a flat velocity dispersion profile with a value of $\sim 100 \text{ km s}^{-1}$.

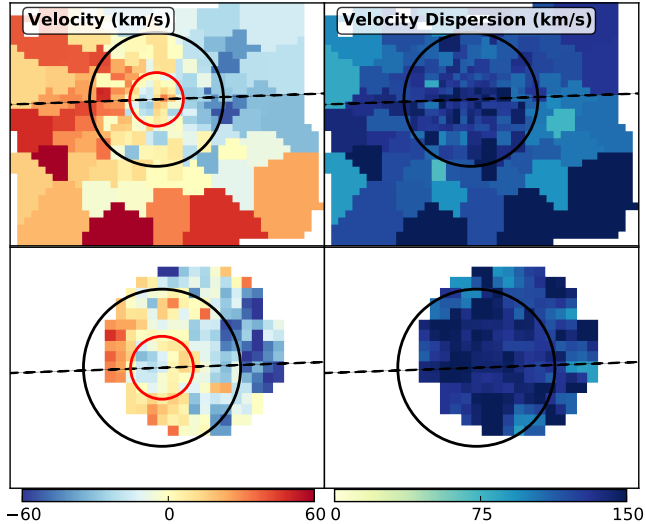


Figure 7. The stellar kinematics maps of NGC1289 as measured by the ATLAS^{3D} survey (top row) and by SAMI (bottom row). In each panel North is up and East to the left. The left hand column shows the velocity maps, scaled to $\pm 60 \text{ km s}^{-1}$ and the right-hand column shows the velocity dispersion, scaled to $0 - 150 \text{ km s}^{-1}$. The black circle shows the SAMI hexabundle field of view, centred on the galaxy (though in this case the observation was not well centred), with a diameter of $\sim 15''$ and the dashed line shows the PA along which the profiles in Figure 8 are extracted. The red circle highlights the kinematically decoupled core in this galaxy. As seen for NGC1665 the structure in the SAMI maps matches that in the ATLAS^{3D} maps.

3.2 NGC 1289

The kinematic maps for NGC1289 are shown in Figure 7. Note that for this object the galaxy was not well-centred in the SAMI hexabundle. As for NGC1665 the structure in the ATLAS^{3D} and SAMI maps is very similar. In particular this galaxy possesses a kinematically decoupled central component (KDC; Krajnović et al. 2011) which is clearly seen in both the ATLAS^{3D} and SAMI velocity maps. The KDC is indicated by the red circle in the velocity maps, shown in the left-hand column of Figure 7.

We extract radial profiles in the same way as for NGC1665, along a line defined by the PA of the galaxy, shown as a dashed black line in Figure 7. The profiles are shown in Figure 8. The presence of the KDC is apparent in both rotation curves in the top panel of Figure 8. The characteristic shape of the inner region of the curve, with a sharp rise and fall, superimposed on a more regular rotation curve clearly indicates a KDC. There is excellent agreement between the ATLAS^{3D} and SAMI data. The velocity dispersion profile also shows good agreement, and in this case SAMI does probe far enough in radius to start to see the same drop off in velocity dispersion seen by ATLAS^{3D}.

The excellent agreement between the new SAMI observations and the ATLAS^{3D} data shows that our observing strategy and data analysis techniques can replicate results from the literature.

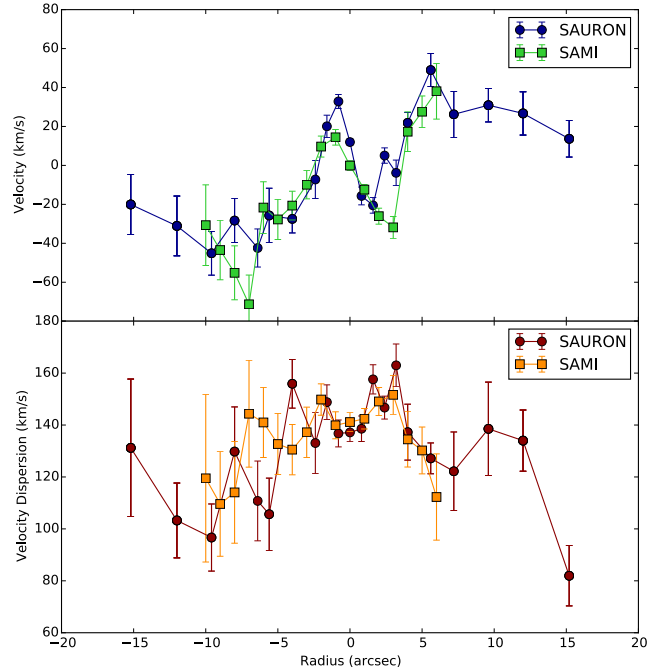


Figure 8. Radial profiles of the kinematics of NGC1289 as measured by ATLAS^{3D} and by SAMI. The curves are as for Figure 6.

4 DERIVED PARAMETERS

4.1 Photometric Parameters

We derive photometric parameters for each galaxy in our sample using the Sloan Digital Sky Survey (SDSS) *r*-band images (Aihara et al. 2011). For the analysis presented here we are interested in the effective radius (R_e), and the ellipticity (ϵ) and photometric position angle (PA_{phot}) measured at the effective radius for each galaxy.

The approach we follow is described in Fogarty et al. (2014). Briefly, we use a Multi Gaussian Expansion (MGE; Emsellem et al. 1994) of the surface brightness profile to derive an accurate measurement of the effective radius of each galaxy. Separately, profiles of the ellipticity and position angle are derived using the IDL routine *find_galaxy.pro* (Krajnović et al. 2011). The ellipticity and position angle at a given radius are determined from the second moments of the luminosity distribution of all connected pixels above a given flux level. The values of R_e , ϵ and PA_{phot} for each galaxy are given in Table A1. The MGE fitting procedure failed for one spiral galaxy in the sample, J215705.29-071411.2, a LTG which is included in Table A1 for completeness but excluded from all subsequent analysis.

4.2 Kinematic Position Angles

To measure the kinematic position angles (PA_{kin}), and associated measurement errors, we use the *fit_kinematic_pa.pro* routine by Michele Cappellari, as outlined in Appendix C of Krajnović et al. (2006). The correct PA is found by comparing a bi-symmetric map based on the data to the data itself and minimising the residuals between the two, while varying the PA of the bi-symmetric map.

The velocity maps and kinematic PAs for the 79 ETGs

in our sample are shown in Figure 12, with the kinematic PAs indicated in black and the photometric PAs in green. In the majority of cases the PAs are well aligned, though in some there is a clear discrepancy. This is discussed further, and quantified, in Section 6. The kinematic positions angles for the entire SAMI Pilot Survey sample are presented in Table A1.

4.3 Calculating λ_R and Kinematic Classification

The kinematic classification of the SAMI Pilot Survey ETGs is discussed extensively in Fogarty et al. (2014). We adopt the ATLAS^{3D} system using the λ_R parameter, a proxy for the luminosity-weighted specific stellar angular momentum for each galaxy within a fiducial radius. λ_R is defined as follows (Emsellem et al. 2007):

$$\lambda_R \equiv \frac{\langle R|V| \rangle}{\langle R\sqrt{V^2 + \sigma^2} \rangle} = \frac{\sum_{i=0}^N F_i R_i |V_i|}{\sum_{i=0}^N F_i R_i \sqrt{V_i^2 + \sigma_i^2}} \quad (2)$$

where F_i , R_i , V_i , σ_i are the flux, radius, velocity and velocity dispersion of the i th of N spaxels included in the sum. Since λ_R is an integrated quantity it must be measured within a fiducial radius. For the SAMI Pilot Survey galaxies we use three fiducial radii, $R_e/2$, R_e , and $2R_e$, chosen according to the size of the galaxy and how that compares to the SAMI field of view and the average seeing for the observations ($1.9'' - 3.0''$). For three of our galaxies λ_R is measured within $2R_e$ and for 15 λ_R is measured within $R_e/2$. For the remainder λ_R is measured within R_e . In Fogarty et al. (2014) we show that this does not impact on our FR/SR classifications. However, when considering the relative values of λ_R for different kinematic classes the aperture effect in λ_R must be addressed. This is discussed in detail in Section 5.1 where we compare the distribution of λ_R between kinematic classes.

For most galaxies in the sample we use the ellipticity and PA_{phot} measured at the fiducial radius to define the ellipse within which λ_R is measured. However, we find seven galaxies with strong bars which compromise the measurements of the galaxy PA_{phot} and ellipticity at the fiducial radius. For those seven objects we use the radial profiles produced as described in Section 4.1 to instead measure the ellipticity and PA_{phot} of the galaxy in the outermost radial bins, away from the influence of the bar.

We classify the ETGs in our sample kinematically, as FRs and SRs, using the dividing line put forward by Emsellem et al. (2011). This framework says that a galaxy is considered a SR if

$$\lambda_R < k\sqrt{\epsilon} \quad (3)$$

where λ_R and ϵ are measured within the same fiducial radius and the proportionality constant k is dependent on the choice of fiducial radius (see Fogarty et al. (2014) for details). We improved our method of fitting kinematics, accounting for possible template mismatch issues (see Section 2.5). Therefore the values of λ_R used here are very slightly different to those reported in Fogarty et al. (2014). The average absolute difference is ~ 0.02 , within the average error on the quantity. This small difference is enough to alter the kinematic classification for two objects in the sample (J011421.54+001046.9 and J011515.78+004555.2). This does not alter any of the results in Fogarty et al. (2014). Here

we use the new values and new kinematic classifications, as reported in Table A1.

The $\lambda_R - \epsilon$ diagram is shown in the left-hand panel of Figure 9. The ETGs are shown as circles and are colour coded according to their kinematic classification, with FRs in blue and SRs in red. Within the ETG sample we find 13 SRs.

For LTGs the classification of FR/SR is less relevant as LTGs are disks and are thus rotation supported systems with high stellar angular momentum. We find that all of the LTGs in our sample unsurprisingly meet the criterion to be classified as FRs (see the left-hand panel of Figure 9). The λ_R values for all of the SAMI Pilot Survey galaxies are given in Table A1.

To avoid confusion, for the remainder of this paper we discuss three different classes of galaxies. The LTGs, visually classified by their morphology; the FRs, first visually classified as ETGs and then further separated on the basis of the $\lambda_R - \epsilon$ diagram; and SRs, again first visually classified as ETG and then further separated kinematically. Thus the ETGs are made up of FRs and SRs and we do not consider any kinematic classification for the LTGs.

5 STELLAR ANGULAR MOMENTUM AS A FUNCTION OF MORPHOLOGICAL TYPE

Understanding the distribution of stellar angular momentum of galaxies with different morphology is crucial to understanding any evolutionary relationship between morphological types. ETGs are thought to form from LTGs through processes as diverse as mild harassment through to disruptive major mergers. How the angular momentum of a galaxy is modified by these processes can help us to determine which processes dominate at which times and in which environments.

We investigate these questions through the λ_R proxy for projected specific stellar angular momentum. In this section we will discuss three classes of galaxies, the ETGs, kinematically separated into SRs and FRs, and the LTGs. The latter category contains 27 out of 106 galaxies in the SAMI Pilot sample for which kinematics are measured. Since this is a small number of galaxies no further subdivision into the usual Sa, Sb, Sc and Sd categories is attempted.

5.1 The Distribution of Stellar Angular Momentum

A histogram of λ_R values for the SRs, FRs and LTGs in the SAMI Pilot Survey sample is shown in the middle panel of Figure 9. The histogram peaks are clearly offset from one another, with median values of λ_R of 0.27 and 0.43 for the FRs and LTGs respectively (we do not discuss the SRs as they are classified using λ_R). A K-S test rejects the hypothesis that the distribution of LTGs and FRs are drawn from the same parent sample, with a p-value of 2×10^{-5} . However, the fraction of LTGs where λ_R is measured at $R_e/2$ is 35%, whereas this fraction is only 0.5% for the FRs, so this direct comparison is not quite fair. Since for both FRs and LTGs the radial λ_R profiles tend to rise quickly in the inner parts comparing our sample of LTGs to a matched sample of FRs where 35% of λ_R values were measured at $R_e/2$ is

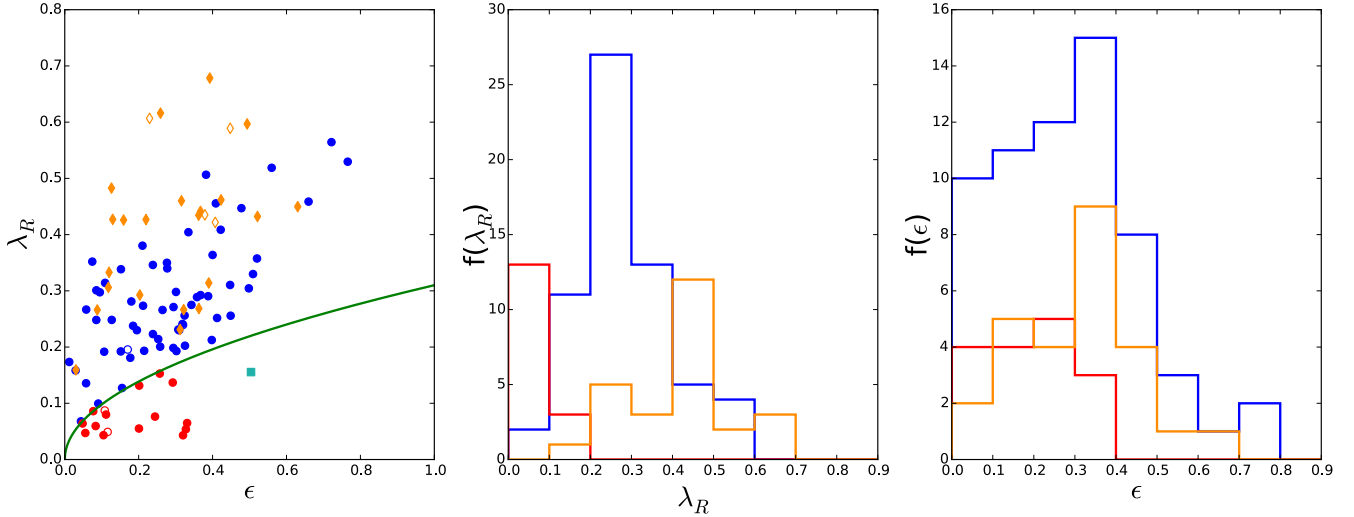


Figure 9. The left panel shows the $\lambda_R - \epsilon$ plot for the SAMI Pilot Survey galaxies. The red and blue points are the ETGs, classified as SRs (red) or FRs (blue). The orange diamonds indicate the LTGs. The turquoise square indicates a single “double sigma” galaxy, a contaminant to the SR population which is not a true SR. The filled symbols represent cluster members and the empty symbols represent non-members. The middle panel shows a histogram of λ_R values for the SAMI Pilot Survey galaxies. The red outline denotes the SRs, the blue the FRs and the orange shows the LTGs. The peaks of the histograms for each class are clearly offset from one another, indicating a change in specific stellar angular momentum between the classes. The right panel shows a histogram of ellipticity values for the SAMI Pilot Survey galaxies, with colours as for the middle panel.

likely to enhance to difference between the two distributions. To test this we measured λ_R at $R_e/2$ for all FRs for which this was feasible and then randomly generated a sample of 63 individual FRs, wherein 35% of the measurements were performed at $R_e/2$. This was repeated 100 times and the resulting average K-S p-value is 4.3×10^{-6} . This implies that there is a systematic difference in stellar angular momentum between the LTGs and the ETGs.

However, λ_R is a projected quantity and so it is possible that the difference in the distribution of λ_R between the LTGs and FRs is simply driven by an underlying difference in the ellipticity distributions of the samples, reflecting an underlying difference in the inclination of the samples. The ellipticity distributions for the LTGs, FRs and SRs are shown in the right-hand panel of Figure 9. The ellipticity distributions of the LTGs and FRs do not match each other closely, though they cannot be ruled out as being the same, with a K-S test yielding a p-value of 0.60. This suggests that although some of the difference in the λ_R distributions of the two samples could be driven by projection effects, it is likely that the LTGs are a class of galaxies with higher specific stellar angular momentum than that of FRs.

Another effect that could drive this difference in λ_R between the LTGs and FRs is a radial variation in mass to light ratio (M/L). This variation is potentially stronger for the LTGs, which tend to be brighter in the outskirts with lower M/L. This could be mitigated by calculating λ_R using a mass weighting rather than a flux weighting. For this work we assume this effect is small and do not implement this correction.

Thus we find that LTGs have the higher angular momentum than the disk-supported ETGs, the FRs. This is expected if the evolution of LTGs to FRs occurs at least partly by dynamical processes such as tidal stripping, interactions or mergers, which can lower stellar angular momentum.

The $\lambda_R - \epsilon$ diagram for the entire sample is shown in the left-hand panel of Figure 9, where the cluster members are shown with filled symbols and the non-members with empty symbols. The difference between the classes of galaxies is less clear here and there is significant overlap between the LTGs and the FRs (seen also in the histograms in the middle and right-hand panels). The locus of points is slightly higher on the plane for the LTGs than the FRs.

5.2 Morphological Transformation

To investigate the distribution of angular momentum more deeply we examine λ_R as a function of galaxy concentration, c , given by the ratio of the r -band Petrosian radius enclosing 90% of the galaxy light to the r -band Petrosian radius enclosing 50% of the galaxy light [$c = R_{90}/R_{50}$, from SDSS DR10; Ahn et al. (2014)]. The choice of photometric band does affect the resulting value for concentration, but we find that using the g , r , or i bands do not remove the trend seen in the $\lambda_R - c$ plane and so we choose r -band for consistency with the rest of our analysis. The results are shown in Figure 10, where, again, cluster members are represented by closed symbols and non-members by open symbols.

There is a trend from LTGs (orange) to FRs (blue) such that the FRs seem to have both lower specific angular momentum and higher concentration values. This is similar to that seen by Falc3n-Barroso et al. (2015) using the CALIFA survey. FRs, being ETGs, will tend to have larger bulge-to-total luminosity ratios than the LTGs and thus higher concentration. The difference in specific angular momentum between the classes could be due to various dynamical processes involved in the formation of FRs from LTGs. The SRs on the other hand, have almost exclusively high concentration and, by definition, low angular momentum.

Figure 10 compares the observational SAMI results with

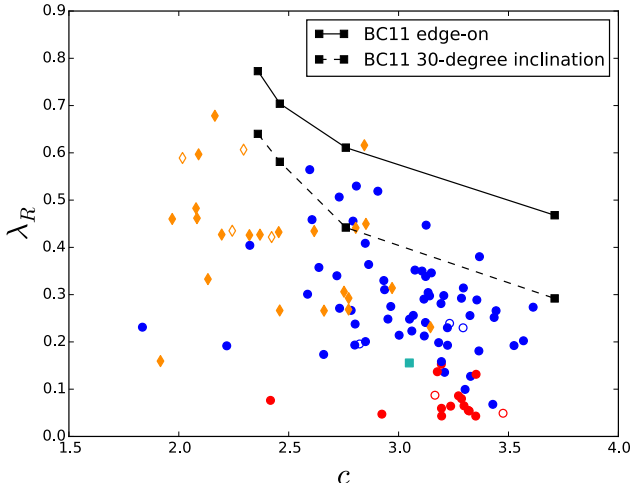


Figure 10. λ_R as a function of concentration for the SAMI Pilot Survey galaxies. The points are colour coded as in the left-hand panel of Figure 9, with filled symbols representing cluster members and empty symbols non-members. The black track shows the evolutionary path of the fiducial model in Bekki & Couch (2011), in which a spiral progenitor is subjected to multiple interactions with other galaxies and is thereby transformed into an S0.

the simulated evolution of a spiral galaxy transforming into an S0 galaxy (FR) (Bekki & Couch 2011) on the $\lambda_R - c$ plane, for two different galaxy inclinations (the edge-on view, shown by the solid black track in Figure 10 and a view with 30° inclination, shown by the the dashed black track). In both cases we plot the results for the fiducial MW-type model from Bekki & Couch (2011) with a total mass of $10^{12} M_\odot$, moving in a group environment with a total mass of $2 \times 10^{13} M_\odot$. In this model the progenitor spiral has a bulge mass which is 17% of the mass of the disk. The c parameter of the simulated FR is derived by estimating a total stellar mass within a given radius (assuming a constant mass-to-light ratio). The spin parameter λ_R for a simulated galaxy ($\lambda_{R,\text{sim}}$) is derived from the simulated stellar kinematics shown in Figure 6 of Bekki & Couch (2011) as follows:

$$\lambda_{R,\text{sim}} = \frac{\sum_{i=0}^N R_i |V_i|}{\sum_{i=0}^N R_i \sqrt{V_i^2 + \sigma_i^2}}, \quad (4)$$

where R_i , V_i , σ_i are the radius, velocity, and velocity dispersion, respectively, for each radial bin. This differs from the calculation of λ_R from observed data as the luminosity factor (F_i in Equation 2) used in the observational λ_R calculation is not included. The stars within $0.2R_d$, where R_d is the initial disk size ($= 17.5$ kpc), are used to derive $\lambda_{R,\text{sim}}$ for the simulated galaxy. The value of $0.2R_d$ is similar to the half-mass radius of the galaxy.

The edge-on model track from Bekki & Couch (2011) (solid line in Figure 10) indicates that the progenitor spiral begins with high λ_R (0.773) and a concentration of $c = 2.36$, with the remnant FR having $\lambda_R = 0.468$ and $c = 3.71$. We have no galaxies in our sample with λ_R as high as the edge-on model spiral, though we do not have any perfectly edge-on systems with which to compare. The dashed line in Figure 10 shows the track for the model with an inclination of 30 degrees. This galaxy starts with $\lambda_R = 0.640$ and the remnant FR has a value of $\lambda_R = 0.292$. This track matches more

closely with our measured points. The initial concentration for the model spiral is close to the median value of 2.42 for our LTG sample (as opposed to a median of 3.12 for the FR sample).

As the model evolves the simulated galaxy loses angular momentum due to repeated interactions with group members. This dynamically heats the galaxy disk causing the line-of-sight velocity to drop and the velocity dispersion to increase, lowering λ_R . By the same mechanism the bulge is grown via multiple episodes of star formation which coincide with galaxy-galaxy interactions (Bekki & Couch 2011), lowering the concentration, c .

Neither of the model tracks match our data exactly, however both exhibit trends in the same direction as the trend between the observed LTG and FR populations. This implies that the formation of some observed FRs could proceed via multiple encounters with other galaxies, as modelled in Bekki & Couch (2011). However, there is a clear overlap between the LTG and FR populations in the $\lambda_R - c$ plane which may be caused by several complicating factors.

Some FRs may not form through harassment (which would lower their angular momentum) but may instead maintain high λ_R throughout their history. A process that could cause this is ram-pressure stripping, which removes gas from a galaxy causing star formation to cease, but does not significantly alter the galaxy dynamics. Many diverse evolutionary links between LTGs and FRs can be imagined and it will take detailed comparison to galaxy formation models to disentangle different effects. Such work is beyond the scope of this paper, but this preliminary result with a small sample of galaxies is promising and indicates that dynamical effects are likely to be important for the formation of at least some of the FR population.

6 KINEMATIC MISALIGNMENT

LTGs and FRs are classes of disk galaxies with many similar properties. SRs, on the other hand, are thought to be a separate class of galaxies with very different intrinsic properties. Krajnović et al. (2011) and Weijmans et al. (2014) find that SRs are not oblate spheroids, like disk galaxies, but show evidence of mildly triaxial figures. This implies that the formation histories of FRs and SRs will likely be different.

We compare the photometric and kinematic PAs (PA_{phot} and PA_{kin}) of the ETGs in the SAMI Pilot sample. A misalignment between these two PAs can be indicative of the intrinsic shape of a galaxy, with oblate spheroids (disks) usually displaying a close alignment between these two quantities. Triaxiality, on the other hand, can introduce a misalignment.

The values of PA_{phot} and PA_{kin} are calculated as described in Section 4. The measurement uncertainties on these quantities are also derived. The mean uncertainty in the photometric PA is 4.1° and the median uncertainty is 2.2° , though there is a tail in the distribution towards large uncertainty. This is a systematic effect as it is difficult to constrain PA_{phot} for objects with lower ellipticity. This is illustrated in the top panel of Figure 11.

Figure 12 shows the kinematic maps for the 79 ETGs, overlaid with their kinematic (black) and photometric PAs (green). The mean uncertainty in the kinematic PA is 6.3°

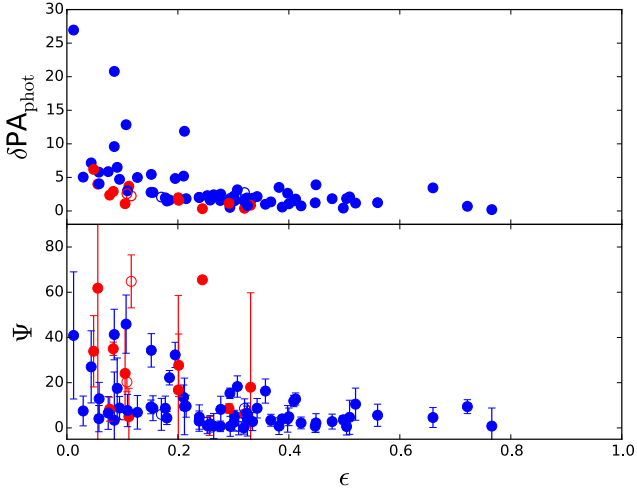


Figure 11. The top panel shows the uncertainty in the measured photometric PA (δPA_{phot}) as a function of ellipticity. There is a systematic trend towards larger uncertainty for rounder galaxies. The bottom panel shows the kinematic misalignment angle Ψ as a function of ellipticity. The FRs are in blue and the SRs in red, with the cluster members indicated by filled symbols and the non-members by empty symbols.

and the median is 3.75° , though as can be seen from Figure 12 there is a large tail in this distribution towards large uncertainty, similar to that seen in the distribution of errors on PA_{phot} . This is also a systematic effect as objects with low or no rotation do not have a well-constrained kinematic PA.

Following Krajnović et al. (2011) and Franx et al. (1991) we calculate the kinematic misalignment angle Ψ for the 79 ETGs in our sample. Ψ is defined as the difference between PA_{phot} and PA_{kin} :

$$\sin \Psi = |\sin(PA_{\text{phot}} - PA_{\text{kin}})|. \quad (5)$$

Using this definition, Ψ lies between 0° and 90° and is insensitive to differences of 180° between the two PAs. The value of Ψ for each of the ETGs is given in Table A1, and Ψ is shown as a function of ellipticity in the bottom panel of Figure 11. A histogram is shown in Figure 13, with the ETGs split kinematically. FRs are shown in blue and SRs in red. A K-S test indicates that the distributions in Ψ are not the same for FRs and SRs with a p-value of 3.2×10^{-3} (if we restrict our analysis to include only those FRs with $\epsilon \leq 0.4$, matching the ellipticity distribution of the SRs, the result stands with a K-S test p-value of 1.2×10^{-2}). This implies that the two classes of galaxies have different distributions in alignment and therefore in intrinsic shape.

In their sample of 260 galaxies from the ATLAS^{3D} survey, Krajnović et al. (2011) found that 90% of galaxies were aligned, with $\Psi < 15^\circ$. If we adopt the ATLAS^{3D} constraint we find that 78% of ETGs have $\Psi < 15^\circ$. However, some galaxies have large error bars on the measured position angles and so we also count as aligned any galaxies where the PA_{phot} and PA_{kin} error bars overlap. This gives us an aligned fraction of 73%. If we split our sample by kinematic class then we find that within the sample of FRs 83% are aligned systems. However, within the SR population the aligned fraction is only 38%.

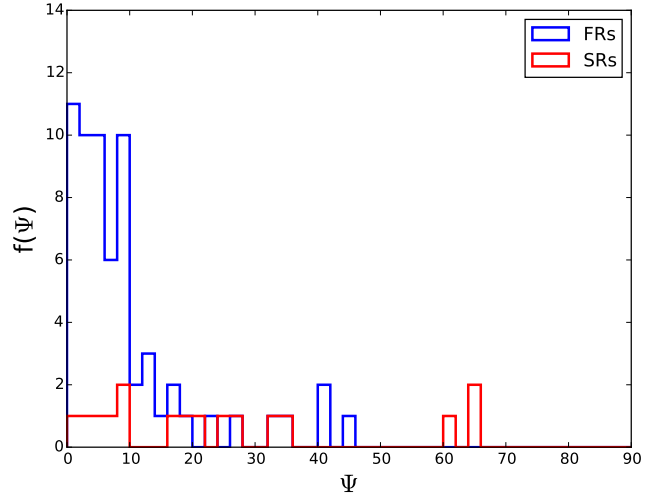


Figure 13. A histogram of the magnitude of kinematic misalignment, Ψ , for the ETGs in the SAMI Pilot sample. The blue histogram indicates the FRs in the sample and the red indicates the SRs.

These results give a strong indication that SRs have an intrinsically different shape distribution than FRs.

7 DISCUSSION

7.1 The Distribution of Angular Momentum

The results presented in Section 5 show that the average measured proxy for projected specific stellar angular momentum, λ_R , is different for FRs and LTGs.

Much work has been done to investigate an evolutionary link between LTGs and FRs (e.g. Gunn & Gott (1972), Larson et al. (1980) and Bekki (1998)). Such an evolutionary link could be one reason for the trend we see from LTGs to FRs in the $\lambda_R - c$ plane.

The overlap between the LTG and FR angular momentum distributions could indicate that there are many mechanisms by which FRs can be formed from LTGs. Different evolutionary paths could affect the position of the remnant galaxy in the $\lambda_R - c$ plane differently.

The example from Bekki & Couch (2011) shown in Figure 10 shows one type of dynamical interaction, namely repeated interactions within a galaxy group, which grows a bulge and changes the angular momentum of a galaxy. Major and minor mergers could have a similar effect, growing a bulge and lowering the angular momentum of the remnant FR (Khochfar et al. 2011; Naab et al. 2013).

Morphological transformation can also occur by secular processes within galaxies. For example, passive fading of LTGs to FRs, by the exhaustion of gas and cessation of SF, will likely create FR remnants with almost unchanged angular momentum, though as λ_R is a flux-weighted quantity it will not be completely unchanged. Passive fading could cause a change in c due to the blue star-forming disk fading, with the underlying bulge component coming to dominate the light. These effects will likely be smaller than those from a merger or other interaction, resulting in little movement in the $\lambda_R - c$ plane as a result.

Disk instabilities can grow a galactic bulge, though a

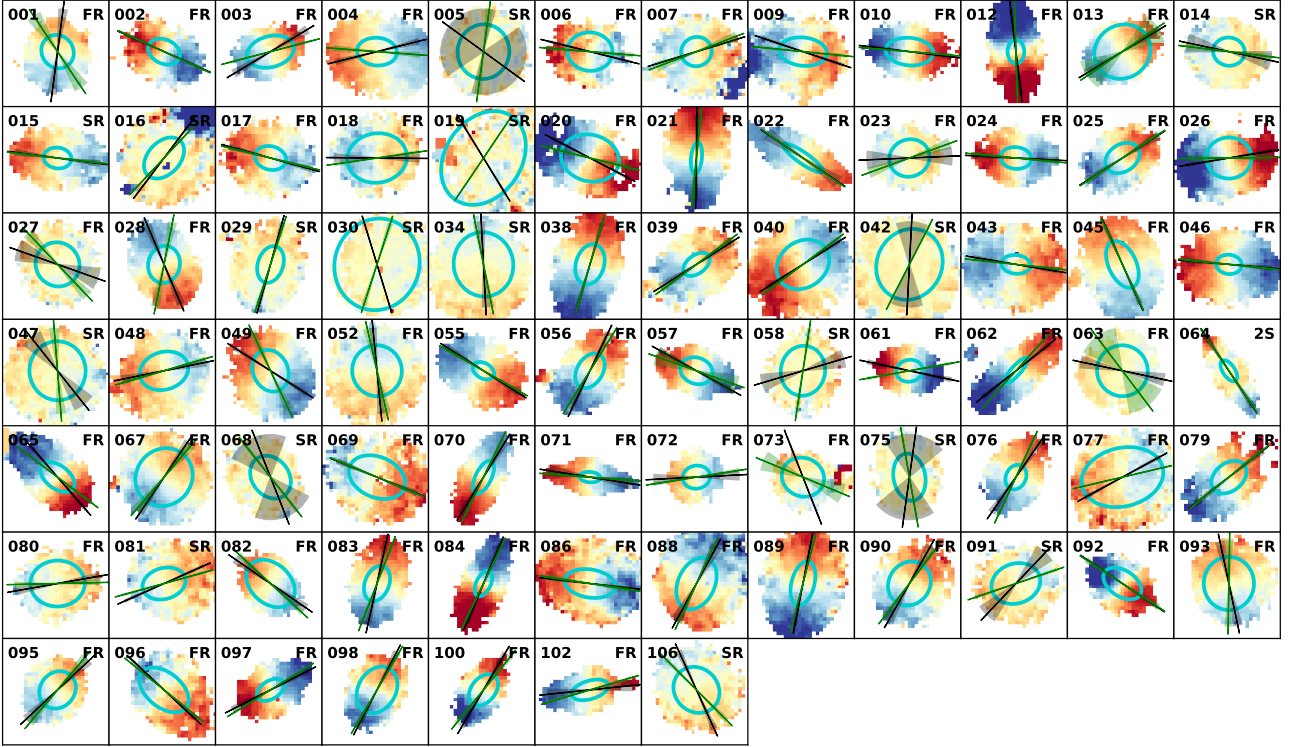


Figure 12. The stellar velocity fields are shown for the 79 ETGs in the SAMI Pilot Survey. For comparison each panel is shown with the same scale, from $-200/+200 \text{ km s}^{-1}$ and in each panel North is up and East is to the left. The black line and shaded black wedge represent the best fit kinematic PA, PA_{kin} , and the measurement error on PA_{kin} respectively. The green line and shaded green wedge represent the best fit photometric PA, PA_{phot} . In each panel the turquoise ellipse represents the fiducial radius within which λ_R was measured. The fiducial radius chosen for each galaxy is shown in Table A1.

bulge generated in this way, a secular bulge, will likely have some different properties to those generated through dynamical interactions (Kormendy & Kennicutt 2004). It is not clear how the processes which create a secular bulge would change the angular momentum of the resulting galaxy. Secularly grown bulges tend to be more disk-like in nature, and have been shown by Fabricius et al. (2012) to have higher rotational support than classical bulges. Thus a galaxy with a secular bulge could end up with higher λ_R for a given concentration than a galaxy with a classical bulge. This may be one way to achieve a large spread in λ_R within LTGs and FRs.

The processes described above illustrate a variety of different evolutionary paths between LTGs and FRs which could account for the observed trend in the $\lambda_R - c$ plane. It is worth noting that the same trend could be seen if galaxies with differing bulge-to-total mass ratios simply have different angular momentum content – with no need for an evolutionary link between the different classes of galaxies. However, the similarity between the trends seen in the model from (Bekki & Couch 2011) and our data indicates morphological transformation through dynamical processes are likely to be important when explaining the distribution of galaxies in the $\lambda_R - c$ plane.

Lastly, different FR formation processes are thought to dominate in different environments. Since our sample consists mostly of cluster member galaxies we cannot explore this further. However, the SAMI Galaxy Survey will have ~ 3400 galaxies, about a quarter of which lie in clusters,

with the remainder occupying smaller groups and the field. With a sample this large it will be possible to construct the $\lambda_R - c$ plane for a range of environments and stellar masses. It may then be possible to isolate the importance of different processes in various environments.

7.2 Galaxy Shapes

In Section 6 we showed that the two kinematic classes of ETGs, the FRs and SRs, have different distributions in misalignment angle, Ψ . The FRs are rotation supported systems with high stellar angular momentum and the majority show close alignment between the kinematic and photometric PAs. This is expected if these galaxies are oblate spheroids.

The SRs on the other hand are pressure-supported systems with low stellar angular momentum. They display a wider range of Ψ values and only 38% are aligned systems. This implies that these galaxies are not oblate spheroids. An intrinsically triaxial shape for these galaxies could cause this.

Our current sample of ETGs is small, so it is difficult to further constrain this problem. This is true especially in the case of SRs, of which we observe only thirteen. Weijmans et al. (2014) perform an inversion of the observed ellipticity distributions for their samples of FRs and SRs from the ATLAS^{3D} survey to probe the intrinsic shape distribution for each class of galaxy. This kind of analysis is not possible with the SAMI Pilot Survey. However as the full SAMI Galaxy Survey will comprise ~ 3400 galaxies, it is expected

that roughly 200 of those likely to be SRs, increasing our current sample by more than an order of magnitude. This will allow a full analysis of the shape distribution of ETGs for a large sample of galaxies.

8 CONCLUSIONS

We present the SAMI Pilot Survey, an IFS survey of 106 galaxies in three galaxy clusters. We have derived stellar velocity and velocity dispersion maps for all 106 galaxies and these are presented in Appendix B.

We also present SAMI observations of two test galaxies drawn from the ATLAS^{3D} survey (NGC1289 and NGC1665). Although the observation procedure was specific to these galaxies the SAMI data reduction procedure could be used with only minor changes. The data were analysed to extract stellar kinematics in the same way as for the SAMI Pilot Survey. The SAMI velocity and velocity dispersion maps of NGC1289 and NGC1665 match those from ATLAS^{3D} extremely well. We conclude that the SAMI data reduction procedure is robust, producing uniform data cubes capable of reproducing known results.

We examine the distribution of angular momentum in our sample using λ_R , a proxy for the projected specific stellar angular momentum in a galaxy. We find that the median λ_R for LTGs is higher than that for FRs, although there is significant overlap between the two populations. We find a trend in the $\lambda_R - c$ plane such that LTGs have higher λ_R and lower concentrations. We suggest that this could be due to an evolutionary link between these groups. The observed trend is consistent with a model wherein a LTG is transformed into a FR through repeated interactions in a group environment. There is a large overlap between the LTG and FR distributions indicating that there are many processes which can affect where a galaxy lies in the $\lambda_R - c$ plane.

We find that a large percentage of the FRs in our sample (83%) show kinematics which are aligned with their photometric PA. This is consistent with their interpretation as oblate spheroids. On the other hand only 38% of the SRs are aligned. This implies that FRs are consistent with being oblate spheroids and SRs are consistent with mild triaxiality.

ACKNOWLEDGEMENTS

The SAMI Galaxy Survey is based on observations made at the Anglo-Australian Telescope. The Sydney-AAO Multi-object Integral field spectrograph (SAMI) was developed jointly by the University of Sydney and the Australian Astronomical Observatory. The SAMI input catalogue is based on data taken from the Sloan Digital Sky Survey, the GAMA Survey and the VST ATLAS Survey. The SAMI Galaxy Survey is funded by the Australian Research Council Centre of Excellence for All-sky Astrophysics (CAASTRO), through project number CE110001020, and other participating institutions. The SAMI Galaxy Survey website is <http://sami-survey.org>.

MSO acknowledges the funding support from the Australian Research Council through a Super Science Fellowship (ARC FS110200023) and through a Future Fellowship (FT140100255).

SMC acknowledges the support of an ARC future fellowship (FT100100457).

JBH acknowledges the support of an Australian Laureate Fellowship.

RCWH was supported by the Science and Technology Facilities Council [STFC grant numbers ST/H002456/1, ST/K00106X/1 & ST/J002216/1].

LC acknowledges support under the Australian Research Councils Discovery Projects funding scheme (project number 130100664).

This work was supported by the Astrophysics at Oxford grants (ST/H002456/1 and ST/K00106X/1) as well as visitors grant (ST/H504862/1) from the UK Science and Technology Facilities Council. RLD acknowledges travel and computer grants from Christ Church, Oxford. RLD is also grateful for support from the Australian Astronomical Observatory Distinguished Visitors programme, the ARC Centre of Excellence for All Sky Astrophysics, and the University of Sydney during a sabbatical visit.

JTA and ISK are the recipients of John Stocker Postdoctoral Fellowships from the Science and Industry Endowment Fund (Australia).

This research made use of Montage, funded by the National Aeronautics and Space Administration's Earth Science Technology Office, Computational Technologies Project, under Cooperative Agreement Number NCC5-626 between NASA and the California Institute of Technology. The code is maintained by the NASA/IPAC Infrared Science Archive.

This research made use of Astropy, a community-developed core Python package for Astronomy (Astropy Collaboration, 2013)

REFERENCES

- Ahn C. P. et al., 2014, *ApJS*, 211, 17
 Aihara H. et al., 2011, *ApJS*, 193, 29
 Allen J. T. et al., 2015, *MNRAS*, 446, 1567
 Allen J. T. et al., 2014, SAMI: Sydney-AAO Multi-object Integral field spectrograph pipeline. Astrophysics Source Code Library
 Bacon R. et al., 2001, *MNRAS*, 326, 23
 Bekki K., 1998, *ApJL*, 502, L133
 Bekki K., Couch W. J., 2011, *MNRAS*, 415, 1783
 Bekki K., Couch W. J., Shioya Y., 2002, *ApJ*, 577, 651
 Bland-Hawthorn J. et al., 2011, *Optics Express*, 19, 2649
 Blanton M. R. et al., 2005, *AJ*, 129, 2562
 Bryant J. J., Bland-Hawthorn J., Fogarty L. M. R., Lawrence J. S., Croom S. M., 2014, *MNRAS*, 438, 869
 Bryant J. J., O'Byrne J. W., Bland-Hawthorn J., Leon-Saval S. G., 2011, *MNRAS*, 797
 Bryant J. J. et al., 2015, *MNRAS*, 447, 2857
 Cappellari M., Emsellem E., 2004, *PASP*, 116, 138
 Cappellari M. et al., 2011a, *MNRAS*, 413, 813
 Cappellari M. et al., 2011b, *MNRAS*, 416, 1680
 Croom S. M. et al., 2012, *MNRAS*, 421, 872
 de Vaucouleurs G., 1959, *Handbuch der Physik*, 53, 275
 Dressler A., 1980, *ApJ*, 236, 351
 Emsellem E. et al., 2011, *MNRAS*, 414, 888
 Emsellem E. et al., 2007, *MNRAS*, 379, 401
 Emsellem E., Monnet G., Bacon R., 1994, *A&A*, 285, 723

- Fabricius M. H., Saglia R. P., Fisher D. B., Drory N., Bender R., Hopp U., 2012, *ApJ*, 754, 67
- Falcón-Barroso J., Lyubenova M., van de Ven G., 2015, in *IAU Symposium*, Vol. 311, IAU Symposium, Cappellari M., Courteau S., eds., pp. 78–81
- Fogarty L. M. R. et al., 2014, *MNRAS*, 443, 485
- Franx M., Illingworth G., de Zeeuw T., 1991, *ApJ*, 383, 112
- Fruchter A. S., Hook R. N., 2002, *PASP*, 114, 144
- Gerhard O. E., 1993, *MNRAS*, 265, 213
- Gunn J. E., Gott, III J. R., 1972, *ApJ*, 176, 1
- Houghton R. C. W., 2015, *MNRAS*, 451, 3427
- Houghton R. C. W. et al., 2013, *MNRAS*, 436, 19
- Hubble E. P., 1926, *ApJ*, 64, 321
- Icke V., 1985, *A&A*, 144, 115
- Khochfar S. et al., 2011, *MNRAS*, 417, 845
- Kormendy J., Kennicutt, Jr. R. C., 2004, *ARA&A*, 42, 603
- Krajnović D., Cappellari M., de Zeeuw P. T., Copin Y., 2006, *MNRAS*, 366, 787
- Krajnović D. et al., 2011, *MNRAS*, 414, 2923
- Larson R. B., Tinsley B. M., Caldwell C. N., 1980, *ApJ*, 237, 692
- Naab T. et al., 2013, *ArXiv e-prints*
- Sánchez-Blázquez P. et al., 2006, *MNRAS*, 371, 703
- Sharp R. et al., 2015, *MNRAS*, 446, 1551
- Sharp R., Birchall M. N., 2010, *PASA*, 27, 91
- Sharp R. et al., 2006, in *Society of Photo-Optical Instrumentation Engineers (SPIE) Conference Series*, Vol. 6269, *Society of Photo-Optical Instrumentation Engineers (SPIE) Conference Series*
- Smith G. A. et al., 2004, in *Society of Photo-Optical Instrumentation Engineers (SPIE) Conference Series*, Vol. 5492, *Society of Photo-Optical Instrumentation Engineers (SPIE) Conference Series*, A. F. M. Moorwood & M. Iye, ed., pp. 410–420
- van der Marel R. P., Franx M., 1993, *ApJ*, 407, 525
- Wang L., Yang X., Luo W., Lau E. T., Wang Y., Mo H. J., van den Bosch F. C., Wang Q. D., 2011, *ArXiv e-prints*
- Weijmans A.-M. et al., 2014, *MNRAS*, 444, 3340

APPENDIX A: THE SAMI PILOT SURVEY GALAXIES

APPENDIX B: STELLAR KINEMATIC MAPS FOR THE SAMI

The *gri* SDSS DR7 images of the SAMI Pilot Survey galaxies are shown in Figure B1. The kinematic maps, derived as described in Section 4 are given in Figures B2 and B3.

Galaxy ID	Galaxy Name	Cluster	m	M_r	ϵ	PA_{phot}	PA_{kin}	Ψ	λ_R	$\Delta\lambda_R$	Galaxy Class	Fiducial Radius
001	J003906.77-084758.3	ABELL0085	1	-20.66	0.085	33.8	172.5	41.3	0.248	0.015	FR	Re
002	J004001.68-095252.5	ABELL0085	1	-21.02	0.276	65.3	66.0	0.7	0.35	0.009	FR	Re
003	J004004.88-090302.6	ABELL0085	1	-20.72	0.358	104.7	121.0	16.3	0.289	0.011	FR	Re
004	J004018.68-085257.1*	ABELL0085	1	-21.45	0.307	85.7	104.0	18.3	0.231	0.013	FR	Re
005	J004046.47-085005.0	ABELL0085	1	-21.04	0.056	172.2	54.0	61.8	0.047	0.009	SR	Re
006	J004101.87-091233.1	ABELL0085	1	-20.78	0.152	85.3	76.0	9.3	0.192	0.012	FR	Re
007	J004112.21-091010.2	ABELL0085	1	-21.02	0.058	111.1	107.0	4.1	0.136	0.007	FR	Re
008	J004112.79-093203.7	ABELL0085	1	-20.67	0.392	102.7	107.0	4.3	0.678	0.064	LTG	Re
009	J004122.06-095240.8	ABELL0085	1	-21.33	0.412	84.3	71.5	12.8	0.252	0.01	FR	Re2
010	J004128.56-093426.7	ABELL0085	1	-20.71	0.422	85.2	83.0	2.2	0.409	0.011	FR	Re
011	J004130.29-091545.8*	ABELL0085	1	-21.39	0.362	3.6	5.0	1.4	0.435	0.023	LTG	Re
012	J004130.42-091406.7	ABELL0085	1	-21.04	0.302	1.7	7.0	5.3	0.193	0.012	FR	Re
013	J004131.25-094151.0	ABELL0085	1	-20.5	0.086	124.4	121.0	3.4	0.301	0.014	FR	Re
014	J004133.41-090923.4	ABELL0085	1	-20.8	0.112	83.0	78.0	5.0	0.08	0.01	SR	Re
015	J004134.89-092150.5	ABELL0085	1	-21.14	0.257	83.4	82.5	0.9	0.153	0.01	SR	Re
016	J004143.00-092621.9	ABELL0085	1	-21.62	0.32	136.8	143.0	6.2	0.043	0.01	SR	Re2
017	J004148.22-091703.1	ABELL0085	1	-20.86	0.258	76.3	74.5	1.8	0.201	0.009	FR	Re
018	J004150.17-092547.4	ABELL0085	1	-21.56	0.177	98.2	89.5	8.7	0.181	0.008	FR	Re
019	J004150.46-091811.2	ABELL0085	1	-22.92	0.244	146.0	31.5	65.5	0.076	0.009	SR	Re2
020	J004152.16-093014.8	ABELL0085	1	-21.36	0.21	76.0	62.5	13.5	0.38	0.008	FR	Re
021	J004153.50-092943.9	ABELL0085	1	-20.9	0.66	174.4	179.0	4.6	0.459	0.013	FR	Re2
022	J004200.64-095004.0	ABELL0085	1	-20.67	0.766	55.2	56.0	0.8	0.53	0.019	FR	Re
023	J004205.86-090240.7	ABELL0085	1	-20.67	0.091	110.0	92.5	17.5	0.1	0.011	FR	Re
024	J004215.91-093252.0	ABELL0085	1	-20.78	0.301	84.5	87.0	2.5	0.298	0.01	FR	Re
025	J004218.75-091528.4	ABELL0085	1	-20.6	0.265	123.3	122.5	0.8	0.266	0.011	FR	Re
026	J004233.86-091040.5	ABELL0085	1	-21.01	0.095	90.7	99.5	8.8	0.297	0.009	FR	Re
027	J004233.99-095442.2	ABELL0085	1	-21.24	0.044	43.5	70.5	27.0	0.068	0.01	FR	Re
028	J004242.26-085528.1	ABELL0085	1	-20.62	0.152	168.7	23.0	34.3	0.338	0.012	FR	Re
029	J004244.68-093316.3	ABELL0085	1	-21.0	0.328	161.9	164.5	2.6	0.054	0.007	SR	Re
030	J004310.12-095141.2	ABELL0085	1	-21.74	0.084	162.0	17.0	35.0	0.06	0.007	SR	Re
031	J011327.21+000908.9	ABELL0168	1	-20.96	0.12	166.7	152.5	14.2	0.333	0.015	LTG	Re2
032	J011346.32+001820.6*	ABELL0168	1	-21.09	0.522	85.1	97.0	11.9	0.432	0.013	LTG	Re2
033	J011415.78+004555.2*	ABELL0168	1	-20.97	0.03	52.1	53.0	0.9	0.159	0.025	LTG	Re
034	J011421.54+001046.9	ABELL0168	1	-21.12	0.077	11.3	3.0	8.3	0.086	0.006	SR	Re
035	J011425.68+003209.9	ABELL0168	1	-20.61	0.316	149.0	10.0	41.0	0.46	0.102	LTG	Re2
036	J011430.80+001928.3*	ABELL0168	1	-21.1	0.088	49.8	21.5	28.3	0.266	0.012	LTG	Re2
037	J011443.86+001709.6	ABELL0168	1	-20.44	0.423	111.8	125.5	13.7	0.462	0.051	LTG	Re2
038	J011446.94+003128.8	ABELL0168	1	-20.68	0.319	163.5	163.5	0.0	0.241	0.006	FR	Re
039	J011454.21+003026.5	ABELL0168	1	-20.43	0.398	126.5	122.5	4.0	0.213	0.011	FR	Re
040	J011454.25+001811.8	ABELL0168	1	-21.01	0.18	126.9	122.5	4.4	0.281	0.006	FR	Re
041	J011456.26+000750.4	ABELL0168	1	-20.79	0.367	154.6	108.5	46.1	0.441	0.013	LTG	Re
042	J011457.59+002550.8	ABELL0168	1	-22.14	0.105	152.9	177.0	24.1	0.043	0.004	SR	Re2
043	J011459.61+001533.1	ABELL0168	1	-20.95	0.368	83.9	80.5	3.4	0.292	0.011	FR	Re
044	J011503.63+002418.7	ABELL0168	1	-21.2	0.363	109.0	110.0	1.0	0.269	0.009	LTG	Re
045	J011507.33+002756.8	ABELL0168	1	-20.55	0.448	24.8	24.0	0.8	0.31	0.009	FR	Re
046	J011508.73+003433.5	ABELL0168	1	-20.76	0.253	84.0	85.0	1.0	0.214	0.012	FR	Re
047	J011515.78+001248.4	ABELL0168	1	-21.15	0.048	4.6	38.5	33.9	0.064	0.007	SR	Re
048	J011516.77+001108.3	ABELL0168	1	-20.81	0.239	106.3	101.5	4.8	0.223	0.008	FR	Re
049	J011531.18+001757.2	ABELL0168	1	-20.92	0.195	25.2	57.5	32.3	0.23	0.007	FR	Re
050	J011603.31-000652.7*	ABELL0168	1	-21.15	0.203	3.0	118.5	64.5	0.293	0.041	LTG	Re
051	J011605.60-000053.6	ABELL0168	1	-21.1	0.63	67.5	71.5	4.0	0.45	0.013	LTG	Re2
052	J011612.79-000628.3	ABELL0168	1	-20.98	0.029	13.0	5.5	7.5	0.158	0.008	FR	Re
053	J011623.61+002644.8	ABELL0168	0	-20.76	0.407	131.1	131.5	0.4	0.422	0.02	LTG	Re
054	J011703.58+000027.4	ABELL0168	1	-20.62	0.39	34.2	1.0	33.2	0.314	0.018	LTG	Re

Galaxy ID	Galaxy Name	Cluster	m	M_r	ϵ	PA_{phot}	PA_{kin}	Ψ	λ_R	$\Delta\lambda_R$	Galaxy Class	Fiducial Radius
055	J215432.20-070924.1	ABELL2399	1	-20.5	0.335	60.3	57.5	2.8	0.404	0.036	FR	Re2
056	J215445.80-072029.2	ABELL2399	1	-20.94	0.324	148.0	154.5	6.5	0.256	0.009	FR	Re
057	J215447.94-074329.7	ABELL2399	1	-20.93	0.212	70.5	61.0	9.5	0.273	0.011	FR	2Re
058	J215457.43-073551.3	ABELL2399	0	-21.52	0.116	171.3	106.5	64.8	0.049	0.009	SR	Re
059	J215556.95-065337.9	ABELL2399	1	-21.6	0.322	122.5	144.5	22.0	0.267	0.022	LTG	Re
060	J215604.08-071938.1	ABELL2399	1	-20.29	0.259	23.4	24.5	1.1	0.616	0.081	LTG	Re
061	J215619.00-075515.6	ABELL2399	1	-20.25	0.185	100.2	78.0	22.2	0.238	0.013	FR	Re
062	J215624.58-081159.8	ABELL2399	1	-20.85	0.722	137.9	128.5	9.4	0.564	0.017	FR	Re
063	J215628.95-074516.1	ABELL2399	1	-20.73	0.012	37.1	78.0	40.9	0.173	0.024	FR	Re
064	J215634.45-075217.5	ABELL2399	1	-20.29	0.504	34.1	33.5	0.6	0.156	0.019	2S	Re
065	J215635.58-075616.9	ABELL2399	1	-20.69	0.409	52.9	41.0	11.9	0.456	0.011	FR	Re
066	J215636.04-065225.6	ABELL2399	1	-20.54	0.494	162.5	167.0	4.5	0.597	0.083	LTG	Re2
067	J215637.29-074043.0	ABELL2399	1	-22.41	0.074	139.4	146.0	6.6	0.352	0.011	FR	Re
068	J215643.13-073259.8	ABELL2399	1	-20.9	0.201	38.3	21.5	16.8	0.055	0.01	SR	Re
069	J215646.76-065650.3	ABELL2399	0	-21.64	0.31	67.3	68.0	0.7	0.23	0.009	FR	Re
070	J215650.44-074111.3	ABELL2399	1	-20.31	0.56	154.1	148.5	5.6	0.519	0.017	FR	Re
071	J215653.48-075405.5	ABELL2399	1	-20.36	0.509	85.7	81.0	4.7	0.33	0.02	FR	Re
072	J215656.92-065751.3	ABELL2399	0	-20.43	0.17	99.0	93.0	6.0	0.196	0.017	FR	Re
073	J215658.25-074910.7	ABELL2399	1	-20.44	0.107	67.4	21.5	45.9	0.192	0.019	FR	Re
074	J215658.51-074843.1	ABELL2399	1	-21.01	0.159	31.5	38.0	6.5	0.426	0.013	LTG	Re
075	J215701.22-075415.2	ABELL2399	1	-20.78	0.331	10.0	172.0	18.0	0.065	0.013	SR	Re
076	J215701.35-074653.3	ABELL2399	1	-20.65	0.215	155.1	145.5	9.6	0.193	0.014	FR	Re
077	J215701.71-075022.5	ABELL2399	1	-22.25	0.294	103.2	118.5	15.3	0.198	0.008	FR	Re
078	J215705.29-071411.2	ABELL2399	1	-20.25	0.0	0.0	158.5	21.5	0	0	-	-
079	J215716.83-075450.5	ABELL2399	1	-20.86	0.294	128.7	128.0	0.7	0.271	0.013	FR	Re
080	J215721.41-074846.8	ABELL2399	1	-20.93	0.155	91.3	100.0	8.7	0.127	0.012	FR	Re
081	J215723.40-075814.0	ABELL2399	1	-21.24	0.292	105.4	114.0	8.6	0.137	0.009	SR	Re
082	J215726.31-075137.7	ABELL2399	1	-20.35	0.277	47.3	55.5	8.2	0.34	0.021	FR	Re
083	J215727.30-073357.6	ABELL2399	1	-20.64	0.343	158.8	167.5	8.7	0.275	0.012	FR	Re
084	J215727.63-074812.8	ABELL2399	1	-20.35	0.478	154.2	157.0	2.8	0.447	0.012	FR	Re
085	J215728.65-073155.4	ABELL2399	1	-20.46	0.118	166.9	11.5	24.6	0.306	0.016	LTG	Re
086	J215729.42-074744.5	ABELL2399	1	-21.74	0.449	81.3	83.5	2.2	0.256	0.008	FR	Re
087	J215733.30-074420.6	ABELL2399	1	-20.88	0.312	24.4	136.5	67.9	0.231	0.012	LTG	Re
088	J215733.47-074739.2	ABELL2399	1	-21.67	0.325	155.2	151.5	3.7	0.202	0.007	FR	Re
089	J215733.72-072729.3	ABELL2399	1	-21.37	0.498	165.4	169.0	3.6	0.304	0.008	FR	Re
090	J215743.17-072347.5	ABELL2399	1	-21.13	0.109	142.8	150.5	7.7	0.314	0.009	FR	Re
091	J215743.24-074545.1	ABELL2399	1	-21.06	0.202	108.8	136.5	27.7	0.131	0.011	SR	Re
092	J215745.05-075701.8	ABELL2399	1	-20.46	0.382	56.8	56.0	0.8	0.506	0.01	FR	2Re
093	J215753.00-074419.0	ABELL2399	1	-21.15	0.058	179.1	12.0	12.9	0.267	0.012	FR	Re
094	J215759.85-072749.5	ABELL2399	1	-21.15	0.126	49.5	32.5	17.0	0.483	0.03	LTG	Re
095	J215806.62-080642.4	ABELL2399	1	-20.59	0.127	139.9	133.0	6.9	0.248	0.012	FR	Re
096	J215807.50-075545.4	ABELL2399	1	-21.31	0.388	51.0	47.0	4.0	0.29	0.012	FR	Re
097	J215810.04-074801.4	ABELL2399	1	-20.58	0.4	121.9	117.0	4.9	0.364	0.016	FR	Re
098	J215811.35-072654.0	ABELL2399	1	-20.44	0.238	149.5	152.5	3.0	0.346	0.012	FR	2Re
099	J215826.28-072154.0	ABELL2399	1	-21.01	0.13	73.2	65.5	7.7	0.427	0.072	LTG	Re2
100	J215840.77-074939.8	ABELL2399	0	-21.05	0.32	140.9	149.5	8.6	0.239	0.017	FR	Re
101	J215853.98-071531.8*	ABELL2399	0	-21.5	0.379	11.1	177.5	13.6	0.435	0.017	LTG	Re2
102	J215902.71-073930.0	ABELL2399	1	-20.28	0.52	106.5	96.0	10.5	0.358	0.019	FR	Re
103	J215910.35-080431.2	ABELL2399	0	-20.99	0.23	96.2	131.5	35.3	0.607	0.02	LTG	Re
104	J215924.41-073442.7	ABELL2399	1	-20.53	0.22	109.9	138.5	28.6	0.427	0.041	LTG	Re
105	J215942.63-073028.6	ABELL2399	0	-20.44	0.448	71.4	89.5	18.1	0.589	0.042	LTG	Re
106	J215945.43-072312.3	ABELL2399	0	-21.45	0.108	44.8	24.5	20.3	0.087	0.009	SR	Re

Table A1. The 106 galaxies in the SAMI Pilot Survey. The first column shows the galaxy ID, the second the galaxy name. The third column shows the cluster sample the galaxy belongs to, while the fourth shows whether the galaxy was deemed to be a cluster member (1) or not (0). The absolute R-band magnitudes used for sample selection are given in column five. These values come from the NYU-VAGC (Blanton et al. 2005). The sixth and seventh columns give the ellipticity and PA. These values are measured at one effective radius, except for those galaxies whose names are marked with a *, which showed strong contamination from bars at one effective radius. In these objects the ellipticity and PA are calculated in the outskirts of the galaxy, away from the influence of the bar. The kinematic PA is given in column eight, with the misalignment angle in column nine. The tenth and eleventh columns show λ_R and the error thereon. The twelfth column gives the kinematic classification for the ETGs and the morphological classification for the LTGs. The final column gives the fiducial radius at which λ_R was measured.

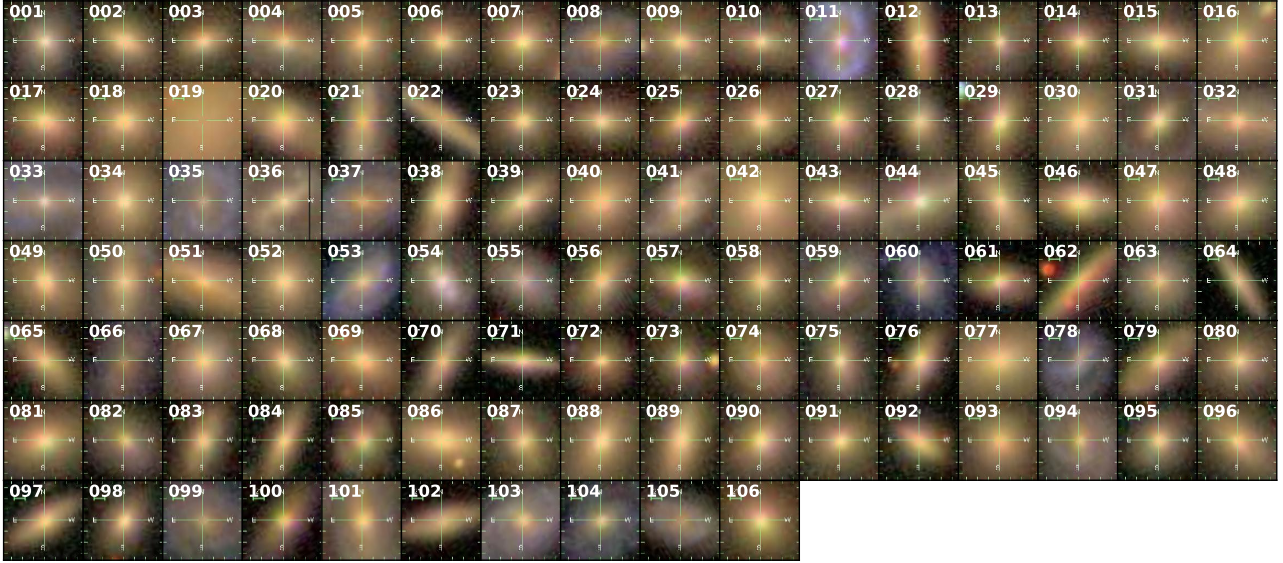


Figure B1. The *gri* SDSS DR7 images for all 106 galaxies in the SAMI Pilot Survey. The galaxy ID shown in the top left of each panel corresponds with that given in Table A1.

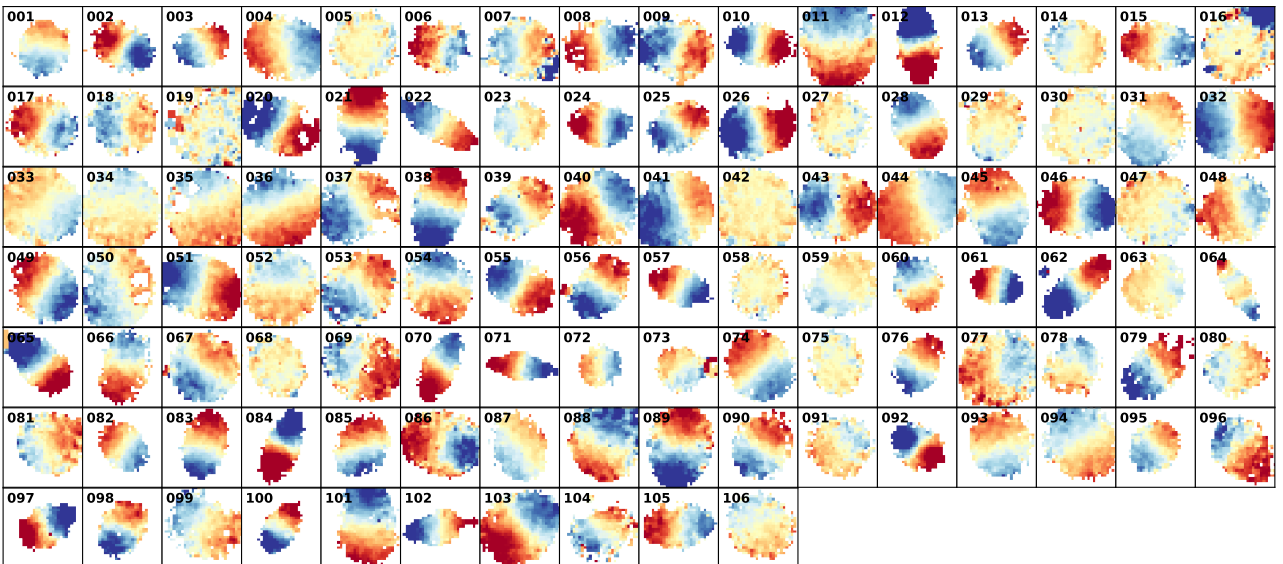


Figure B2. The stellar velocity maps for all 106 galaxies in the SAMI Pilot Survey. The galaxy ID shown in the top left of each panel corresponds with that given in Table A1. The maps are all scaled to between $\pm 150 \text{ km s}^{-1}$. Each panel is 15 arcseconds on a side.

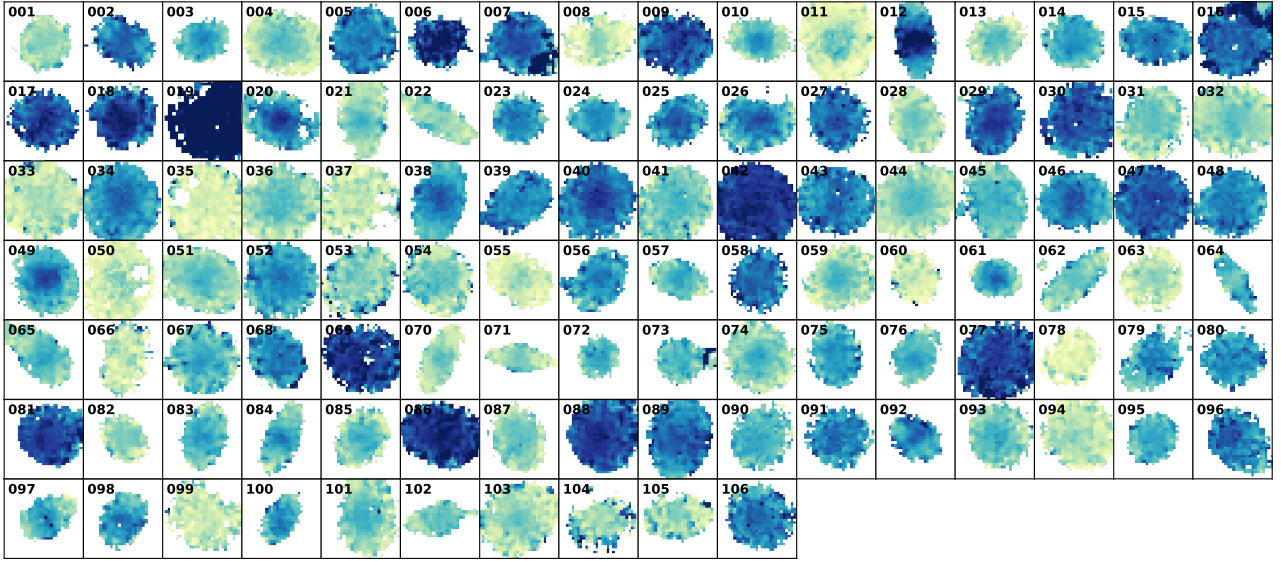


Figure B3. The stellar velocity dispersion maps for all 106 galaxies in the SAMI Pilot Survey. The galaxy ID shown in the top left of each panel corresponds with that given in Table A1. The maps are all scaled to between $0 - 300\text{km s}^{-1}$. Each panel is 15 arcseconds on a side.